# Magnetic confinement of a neutral atom in a double-wire waveguide: A nonlinear dynamics approach.

J. Pablo Salas,[1] Manuel Iñarrea,[1] Víctor Lanchares,[2] Jesús Palacián,[3] and Patricia Yanguas[3]

[1] *Área de Física, Universidad de La Rioja, 26006 Logroño, La Rioja, Spain*

[2] *Departamento de Matemáticas y Computación, Universidad de La Rioja, 26006 Logroño, La Rioja, Spain*

[3] *Departamento de Estadística, Informática y Matemáticas and Institute for Advanced Materials and Mathematics, Universidad Pública de Navarra, 31006 Pamplona, Spain*

(Dated: February 15, 2022)

## Abstract

In this paper we focus on the classical dynamics of a neutral atom trapped in a double-wire waveguide in the presence of two uniform bias fields. Because the trapping region takes place in a plane perpendicular to the (parallel) wires, the dynamics is governed by a two-degrees of freedom Hamiltonian where, besides the energy, the two bias fields are the relevant system's parameters. An exhaustive study of the critical points of the potential energy surface, their stability and bifurcations is carried out, so that, two different trapping regions are characterized. The dynamics in each of these regions is studied by applying classical perturbation theory, which provides an integrable approximation of the original Hamiltonian. The dynamics arising from this normalized Hamiltonian (stability of the equilibrium points, their bifurcations and the phase flow evolution) is then analyzed in a convenient set of phase variables. Poincaré surfaces of section to describe the structure and evolution of the phase space governed by the full Hamiltonian are also used. A complete agreement between the descriptions of the dynamics provided by the perturbation theory and the numerical studies is obtained.

PACS numbers: **37.10.Gh 05.45.-a 52.55.-s**

## I. INTRODUCTION

Experimental magnetic trapping of neutral atoms was reported for the first time in 1985 [1]. Since then, the magnetic confinement of neutral atoms has become a well-known and widespread technique that, among other things, has contributed to the experimental achievement and manipulation of Bose-Einstein condensates [2–7]. The key point that makes atom trapping possible is the interaction of its magnetic moment with a non-uniform magnetic field. Because this interaction is very weak, the atoms to be trapped have to be previously cooled at microkelvin temperatures and below.

Two significant examples of magnetic traps are the quadrupole and the Ioffe traps [1, 8–10]. The quadrupole trap consists of two Helmholtz coils with currents in opposite directions, while the Ioffe trap consists of four straight currents plus two Helmholtz coils. In any case, conventional magnetic traps are always macroscopic devices made of coils and/or current conductors. A detailed theoretical study of several confining magnetic field configurations for neutral atoms can be found in [8].

A different perspective for neutral atom trapping is provided by microtraps, which are magnetic traps on a microscopic scale. Based on the same physics, these microtraps are made of electric conductors integrated on a substrate, i.e., they are magnetic traps on microchips. For more information about microtraps for neutral atoms, we refer the reader to [11, 12]. The first purpose of microtraps was the achievement of strong three-dimensional confinement. However, the great versatility of the lithographic methods used for the fabrication of these microtraps made possible to use them as atom waveguides. Roughly speaking, atom waveguides are miniaturized current carrying structures that only provide strong atom confining in the transverse plane of the currents. In particular, a single straight current is the simplest magnetic waveguide because, due to the atoms are trapped in the plane radial to the current, an effective guiding is obtained along the longitudinal direction defined by the wire [13–17]. In general, the ability to design magnetic waveguides with a wide variety of geometries allows in turns to manipulate matter in very different ways. For example, Bose-Einstein condensates and degenerate Fermi gases can be loaded and manipulated in magnetic waveguides [18–21]. Interestingly, submicron magnetic lattices are a nice alternative to optical lattices for trapping ultracold atoms [22, 23].

Even in the simplest magnetic trap, the trapping potential is highly non-linear, which

makes the classical dynamics of these systems very attractive. In this sense, although classical studies are very scarce, the different trapping designs described previously have been considered in the literature. Indeed, Bergeman [6, 24**?** ] and Gomer *et al.* [25] found that, for high energy, the motion of an atom trapped in a quadrupolar trap is chaotic. For the same trap configuration, Salas and Iñarrea [26] carried out an exhaustive numerical study of the evolution and structure of the phase space. Surkov et al. [27] studied analytical and numerically the motion of a neutral particle in a Ioffe trap. Signatures of chaotic dynamics of a Bose-Einstein condensate loaded in a magnetic waveguide have been found in [19]. More recently, the dynamical tunneling of ultracold atoms in a magnetic microtrap has been investigated in [28], and the existence of guiding stability domains in a magnetic waveguide was showed by Alzar [29].

In order for classical dynamics to have a more relevant role in this subject, the main goal of this paper is to get further insight about the dynamics of a neutral atom confined in a magnetic waveguide. More specifically, we focus on a double-wire waveguide in the presence of two uniform bias fields. We choose a double-wire geometry because the trapping potential of this configuration is, at the same time, complex enough to offer different trapping configurations [30] and simple enough to be mathematically manageable.

The paper is organized as follows. In Sec. II, we assume the adiabatic approximation to state the trapping potential created by the double-wire waveguide in the presence of two uniform bias fields. Assuming the wires are parallel, and that they are located on the $x$-$z$ plane, the external bias fields $b_x$ and $b_z$ are added along the $x$ and the $z$ axes, respectively. The corresponding two-degrees of freedom Hamiltonian governing the dynamics of the atom is then established. After introducing a convenient set of units, besides the energy, we get that the relevant parameters in the Hamiltonian controlling the dynamics are the dimensionless versions of the two bias fields. In Sec. III we carry out a comprehensive study of the critical points (equilibrium points) of the system's potential, their stability and bifurcations. From this study, we find that, depending on whether $b_x < 1$ or $b_x > 1$, two different trapping regions are possible. In Sec. IV we focus on the dynamics when $b_x < 1$. This study is carried out in two different and complementary ways. On the one side, we apply classical perturbation theory to compute an integrable approximation to the original Hamiltonian. We use this normalised Hamiltonian to analyze the stability of the

equilibrium points, their bifurcations and the phase flow evolution. On the other side, we compute Poincaré surfaces of section to describe the structure and evolution of the phase space governed by the original Hamiltonian. We obtain a complete agreement between both descriptions of the dynamics. In Sec. V we carry out the same investigation as in Sec. IV but for $b_x > 1$. Finally, the conclusions are provided in Sec. VI.

## II. THE CONFINING POTENTIAL AND THE HAMILTONIAN

Let us consider a neutral atom in the vicinity of a given waveguide. Under the adiabatic approximation, the atom will remain in a fixed Zeeman sublevel $m_F$ and the potential $V(r)$ responsible for the interaction between the atom and the magnetic field $\vec{B}$ of the waveguide is given by [5]:

$$V(r) \approx \mu_{ef}\ |\vec{B}(r)|, \quad \mu_{ef} = \mu_B\ g\ m_F, \tag{1}$$

where $g$ is the $g$-factor and $\mu_B$ is the Bohr magneton. From Eq. (1) we observe that trappable states are those such that $m_F > 0$ (low-field seeking states) [5].

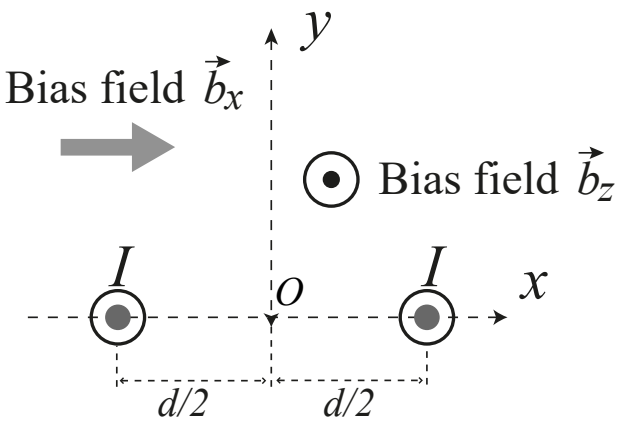


FIG. 1. Atom waveguide using two wires carrying equal currents $I$ and two bias magnetic fields.

In particular, we consider a double-wire waveguide [12–17] made of two parallel wires separated by a distance $d$ and carrying co-propagating equal currents $I$ (see Fig.1), so that the $x$-$z$ plane contains the wires, which are located along the $z$ axis. If just this two wires configuration is considered, magnetic confinement takes place around the origin $O$ and, because the total magnetic field at the center of the trap $O$ is zero, the minimum of the potential in this trap is zero. Thence, atoms near the center of the trap may undergo Majorana spin

flips [31, 32] and leave the trap. In order to avoid these Majorana losses, a bias magnetic field $\vec{b}_z = b_z\widehat{z}$, parallel to the $z$ axis, is added (see Fig.1). Furthermore, for technical reasons in the design of the trap, it is convenient to maintain the potential minimum of the system away from the $y = 0$ plane defined by the wires. In this way, a bias magnetic field $\vec{b}_x = b_x\widehat{x}$, parallel to the $x$ axis is also added (see Fig.1), so that the center of the trap is now off the $y = 0$ plane [12].

For the configuration depicted in Fig.1, and using Cartesian coordinates, the total magnetic field $\vec{B}$ created by the waveguide is given by:

$$\vec{B} = (B_x, B_y, B_z), \tag{2}$$

$$B_x = b_x - \frac{I\mu_o y}{2\pi[(x - d/2)^2 + y^2]} - \frac{I\mu_o y}{2\pi[(x + d/2)^2 + y^2]}, \tag{3}$$

$$B_y = \frac{I\mu_o(x - d/2)}{2\pi[(x - d/2)^2 + y^2]} + \frac{I\mu_o(x + d/2)}{2\pi[(x + d/2)^2 + y^2]}, \tag{4}$$

$$B_z = b_z, \tag{5}$$

where $\mu_o$ is the magnetic permeability of the vacuum. In Cartesian variables, for an atom of mass $m$, the Hamiltonian of the system reads as:

$$\mathcal{H} = \frac{p_x^2 + p_y^2 + p_z^2}{2m} + V, \tag{6}$$

where, using the above expressions for $\vec{B} = (B_x, B_y, B_z)$, the total interaction potential $V$ is given by:

$$V \equiv V(x, y) = \mu_{ef}\ |\vec{B}(r)| = \mu_{ef}\sqrt{B_x^2 + B_y^2 + B_z^2}. \tag{7}$$

As the $z$-coordinate is cyclic in Hamiltonian (6), the relevant dynamics of the system takes place in the $x$-$y$ plane perpendicular to the wires. If we reduce to that plane, the Hamiltonian becomes

$$\mathcal{H} = \frac{p_x^2 + p_y^2}{2m} + V(x, y), \tag{8}$$

and we are dealing with a two-degrees of freedom Hamiltonian system. Besides the energy $\mathcal{H} = E$, the dynamics depends on the external parameters $m$, $\mu_{ef}$, $I$, $d$, $b_x$ and $b_z$, that is to say, on the kind of atom and on the geometry of the waveguide. Following Ref. [30], it is possible to reduce the number of the external parameters by using the dimensionless lengths $(x', y') = (2x/d, 2y/d)$ and the dimensionless time $t' = t\ \nu$, with $\nu$ being the frequency

$$\nu = \sqrt{\frac{4\mu_{ef}B_o}{md^2}}, \qquad B_o = \frac{\mu_o\ I}{\pi\ d}.$$

Applying these transformations to (8), and after dropping primes, we arrive at the following dimensionless Hamiltonian:

$$E = \mathcal{H} \equiv \frac{\mathcal{H}}{\mu_{ef}\ B_o} = \frac{p_x^2 + p_y^2}{2} + V(x, y), \tag{9}$$

where the energy of the system is measured in units of $E_o = \mu_{ef} B_o$, and $V(x, y)$ is converted into

$$V(x, y) = \sqrt{\left(b_x - \frac{y}{f_1(x, y)} - \frac{y}{f_2(x, y)}\right)^2 + b_z^2 + \left(\frac{x+1}{f_1(x, y)} + \frac{x-1}{f_2(x, y)}\right)^2}, \tag{10}$$

with $f_1(x, y) = [(x + 1)^2 + y^2]$, $f_2(x, y) = [(x - 1)^2 + y^2]$, and where the bias fields $b_x$ and $b_z$ are measured in units of $B_o$. Then, besides the (dimensionless) energy $E$, the system depends on the external parameters $b_{x,z}$. At this point we note that it is easy to check that the potential $V(x, y)$ given by (10) enjoys the symmetry $x \to -x$, i.e., it is symmetric with respect the $y$ axis.

The Hamiltonian equations of motion arising from (9) are:

$$\begin{aligned} &\dot{x} = p_x, \quad \dot{y} = p_y, \\ &\dot{p}_x = -\frac{\partial V(x, y)}{\partial x}, \quad \dot{p}_y = -\frac{\partial V(x, y)}{\partial y}. \end{aligned} \tag{11}$$

It is straightforward to check that rectilinear orbits along the $y$ axis are particular solutions of (11). We name these rectilinear orbits as $I_y$. Note that the equilibrium points of the Hamiltonian flow (11) are the critical points of the potential $V(x, y)$ together with the conditions $p_x = p_y = 0$.

## III. THE CRITICAL POINTS OF THE POTENTIAL

Most of the trapping features of this magnetic guide can be obtained from the landscape of the potential energy surface (10), which is mainly determined by the critical points. The landscape of the potential $V(x, y)$ has been studied in [30] when only the bias field $b_x$ along the $x$ axis is present. Here, we revisit and complete that study considering the additional bias field $b_z$ along the $z$ axis. The critical points of $V(x, y)$ are the roots of the following equations:

$$\frac{\partial V(x, y)}{\partial x} = 0, \quad \frac{\partial V(x, y)}{\partial y} = 0. \tag{12}$$

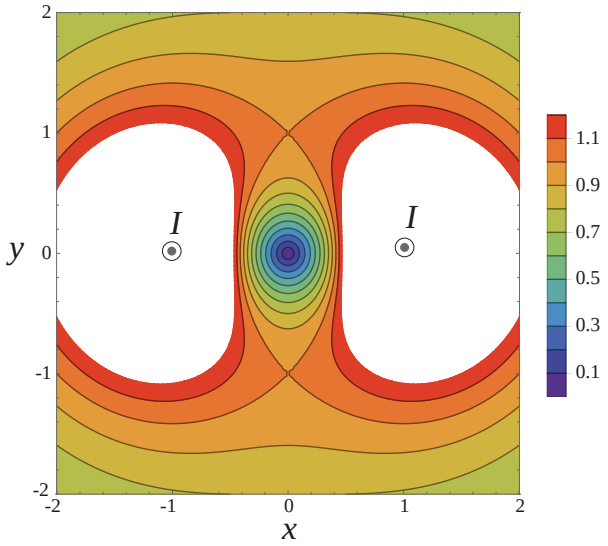


FIG. 2. Equipotential curves of the potential energy surface $V(x, y)$ when there are no bias magnetic fields, i.e., when $b_x = b_z = 0$.

It is easy to see that critical points only depend on the value of $b_x$, while their energies depend also on $b_z$. We consider two cases:

When there are no bias magnetic fields, although at the origin $P_1 = (0, 0)$ the derivatives of the potential are not defined, there is a potential well of energy $E_1 = 0$. Besides this potential well, there are two equilibrium points $P_2 = (0, 1)$ and $P_3 = (0, -1)$ located on the $y$ axis and with equal energy $E_2 = E_3 = 1$. It is straightforward to show that $P_{2,3}$ are saddle points, and thence, the potential energy surface $V(x, y)$ for $b_x = b_z = 0$ shows the landscape depicted in Fig. 2. Note that the depth of the potential well is $\Delta E = 1$ and the only trapping region is around the origin.

When the two bias magnetic fields are present, Eqs. (12) admit six possible solutions, that include those for $b_x = b_z = 0$. These equilibria, as well as their existence conditions, stability and energies, are detailed in Table I. Note that, due to the symmetry of the potential $V(x, y)$ with respect to the $y$ axis, the critical points always appear in symmetric pairs with respect to that axis. The position and stability of the equilibria only depend on the value of $b_x$, while the energy also depends on $b_z$. This is not a surprising result because, as we noted in Sec.II, the bias field $b_x$ was added in order to move the potential minimum of the trap away from the $y = 0$ plane, while the role of the field $b_z$ is to prevent a zero magnetic field at the center of the trap. Therefore, it is expected that the positions of the critical points depend

| Equilibrium | Existence | Stability | Energy |
|---|---|---|---|
| $P_1 = (0, (1 - \sqrt{1 - b_x^2})/b_x)$ | $0 \leq b_x \leq 1$ | Minimum | $E_1 = b_z$ |
| $P_2 = (0, 1)$ | Always | S.P. | $E_2 = \sqrt{(1 - b_x)^2 + b_z^2}$ |
| $P_3 = (0, -1)$ | Always | S.P. | $E_3 = \sqrt{(1 + b_x)^2 + b_z^2}$ |
| $P_4 = (0,\ (1 + \sqrt{1 - b_x^2})/b_x)$ | $0 < b_x \leq 1$ | Minimum | $E_4 = b_z$ |
| $P_{5,6} = (\pm\sqrt{1 - 1/b_x^2},\ 1/b_x)$ | $b_x \geq 1$ | Minima | $E_{5,6} = b_z$ |

Table I. Conditions of existence, stability and energy of the critical points of $V(x, y)$. The saddle points are denoted by S.P.

only on $b_x$, while their energies depend on both $b_x$ and $b_z$.

In the interval $0 < b_x < 1$, only the equilibria $P_{1,2,3,4}$ along the $y$ axis exist, in such a way that the minima $P_1$ and $P_4$ determine two trapping regions along the $y$ axis. Although of equal depth $\Delta E = E_2 - E_{1,4}$, the potential well associated to $P_4$ is wider than the potential well associated to $P_1$, so that a tighter binding is provided by the potential well associated to $P_1$. Furthermore, for a constant value of $b_x(b_z)$, the depth $\Delta E$ of the potential wells decreases for increasing $b_z(b_x)$. As an example, the left panel of Fig. 3 shows the potential energy surface $V(x, y)$ along the $x = 0$ direction for four representative values of $b_x$ and $b_z$. In the right panel of Fig. 3 the landscape of $V(x, y)$ for $b_x = 0.5$ and $b_z = 0.1$ is depicted, where the main features above described can be observed.

When $b_x = 1$, the equilibria $P_1$, $P_2$ and $P_4$ collide and, for $b_x > 1$, only the saddle point $P_2$ survives and the minima $P_{5,6}$, located along the unit circle $x^2 + y^2 = 1$, appear. As an example, in Fig. 4 the equipotential curves of $V(x, y)$ for $b_x = 1.25$ and $b_z = 0.1$ are shown. We remark here that the potential landscape for $b_x > 1$ opens the nice possibility to get a twofold guide whose position along the unit circle can be tuned by varying the bias field $b_x$ [30].

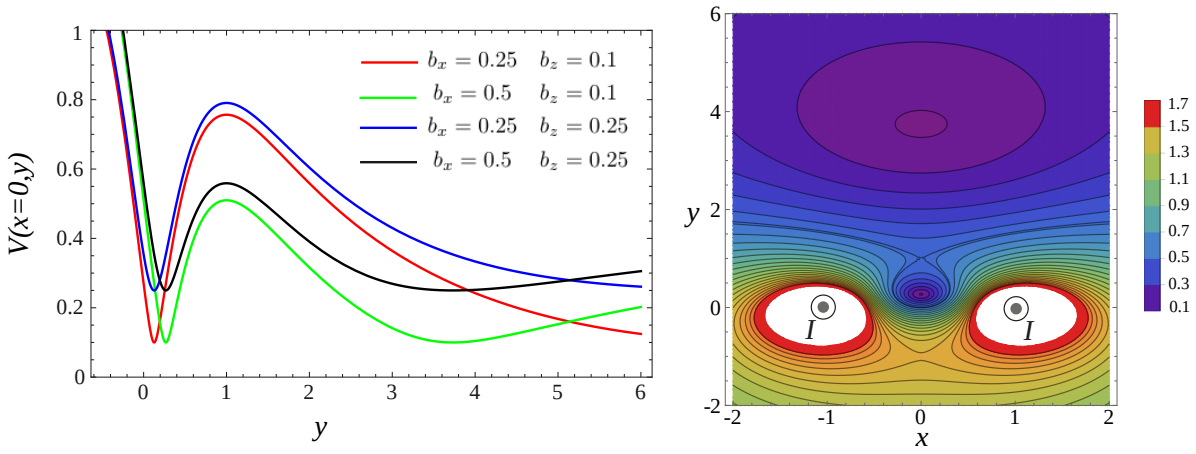


FIG. 3. Left panel: Potential $V(x, y)$ along the $x = 0$ direction for $b_x = 0.25$ and $b_z = 0.1$ (red curve), for $b_x = 0.5$ and $b_z = 0.1$ (green curve), for $b_x = 0.25$ and $b_z = 0.25$ (blue curve) and for $b_x = 0.5$ and $b_z = 0.25$ (black curve). Right panel: Equipotential curves of the potential energy surface $V(x, y)$ for $b_x = 0.5$ and $b_z = 0.1$.

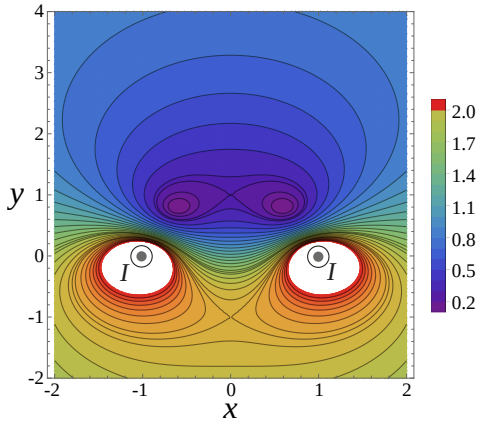


FIG. 4. Equipotential curves of the potential energy surface $V(x, y)$ for $b_x = 1.25$ and $b_z = 0.1$.

## IV. DYNAMICS FOR THE CASE $0 < b_x < 1$

For $0 < b_x < 1$, the landscape of the potential $V(x, y)$ is characterized by the presence of two potential wells around the minima $P_1$ and $P_4$, which are separated by the the saddle point $P_2$. Because both equilibria are located along the $x = 0$ axis with coordinates $y_{1,4} = (1 \mp \sqrt{1 - b_x^2})/b_x$ the perturbative study of this section can be formally carried out simultaneously for both potential wells. Then, we start the study of this section moving the equilibria $P_{1,4}$

to the origin by means of the canonical transformation

$$x \to x', \quad y \to y' + y_o, \quad p_x \to p'_x, \quad p_y \to p'_y,$$

where $y_o = y_{1,4}$ is the $y$-coordinate of $P_1$ or $P_4$ (see Table I). After dropping primes in the new variables $(x', y', p'_x, p'_y)$, Hamiltonian (9) becomes

$$\mathcal{H} = \frac{p_x^2 + p_y^2}{2} + \sqrt{\left(b_x - \frac{y + y_o}{g_1(x,y)} - \frac{y + y_o}{g_2(x,y)}\right)^2 + b_z^2 + \left(\frac{x+1}{g_1(x,y)} + \frac{x-1}{g_2(x,y)}\right)^2}, \tag{13}$$

where $g_1(x,y) = [(x+1)^2 + (y+y_o)^2]$, $g_2(x,y) = [(x-1)^2 + (y+y_o)^2]$. Now, and when the atom is trapped in either of the potential wells located around $P_1$ or $P_4$ (i.e., when the energy is below the energy $E_2$ of the saddle point $P_2$), we can expand Hamiltonian (13) in a Taylor series around the minimum $P_1$ or $P_4$:

$$\mathcal{H} = b_z + \frac{p_x^2 + p_y^2}{2} + \frac{\omega^2}{2}(x^2 + y^2) + \alpha\ y(x^2 + y^2) + (x^2 + y^2)(\beta_1 x^2 + \beta_2 y^2) + \cdots, \tag{14}$$

where the constant term $b_z$ is the energy of the minima $P_{1,4}$. We observe that the quadratic part of the expansion corresponds to a two dimensional elliptic (isotropic) harmonic oscillator of frequency $\omega$ given by

$$\omega = \frac{2|1 - y_o^2|}{(y_o^2 + 1)^2 \sqrt{b_z}}, \tag{15}$$

which provides the linear approximation of the frequency and period $\tau = 2\pi/\omega$ of the two linear modes, namely the oscillations along the $x$ and $y$ axis, respectively.

### A. The Linear Approximation

The linear approximation is the lowest order of any perturbation theory. Thence, we briefly focus on the behavior of our system when just the quadratic part of the expansion (14) is considered. In particular, it is very interesting to compare the frequencies around both potential wells. From (15), the ratio $\eta = \omega_1/\omega_4$ between the frequencies $\omega_1$ and $\omega_4$ around the inner and the outer potential wells (i.e., when $y_o = y_1 = (1 - \sqrt{1 - b_x^2})/b_x$ and $y_o = y_4 = (1 + \sqrt{1 - b_x^2})/b_x$ respectively) does only depend on the value of $b_x$. When this ratio $\eta$ is plotted for $0 < b_x < 1$ (see Fig.5), we find that, up to $b_x \lesssim 0.5750$, the value of $\omega_1$ is much larger than 10 times the value of $\omega_4$, and that only for values of $0.9428 \lesssim b_x \lesssim 1$ both frequencies take similar values. Indeed, we have that the dynamics is, in general,

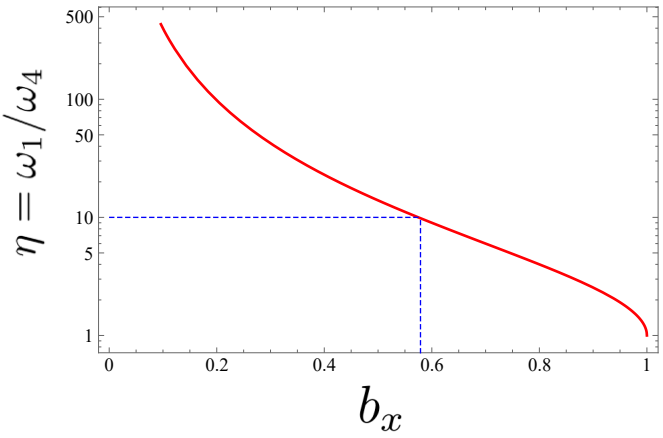


FIG. 5. Frequency ratio $\eta = \omega_1/\omega_4$ between the frequencies $\omega_1$ and $\omega_4$ around the inner and the outer potential wells (i.e., when $y_o = y_1 = (1 - \sqrt{1 - b_x^2})/b_x$ and $y_o = y_4 = (1 + \sqrt{1 - b_x^2})/b_x$ respectively). The dashed blue lines mark the value of $b_x \approx 0.5750$ for which the frequency ratio is $\eta = 10$. Note that a logarithmic scale is used in the vertical axis.

much faster around the minimum $P_1$ than around the minimum $P_4$, which is the expected behavior because, as we found in Sec. III, a tighter confinement is provided by the potential well associated to $P_1$.

### B. Classical Perturbation Theory beyond the Linear Approximation

Hamiltonian (14) can be written as the sum

$$\mathcal{H} = b_z + \mathcal{H}_0 + \mathcal{H}_1, \tag{16}$$

$$\mathcal{H}_1 = \sum_{n\geq 3} \mathcal{P}_n = \alpha\ y(x^2 + y^2) + (x^2 + y^2)(\beta_1 x^2 + \beta_2 y^2) + \cdots, \tag{17}$$

where $\mathcal{H}_0$ stands for the elliptic oscillator,

$$\mathcal{H}_0 = \frac{p_x^2 + p_y^2}{2} + \frac{\omega^2}{2}(x^2 + y^2), \tag{18}$$

and $\mathcal{P}_n$ are homogeneous polynomials of degree $n$ resulting from the Taylor expansion, where

$$\alpha = \frac{4y_o\left(y_o^2-3\right)\left(1-y_o^2\right)}{b_z\left(y_o^2+1\right)^5},$$

$$\beta_1 = \frac{2b_z^2\left(y_o^2+1\right)^2\left(-y_o^6+8y_o^4-5y_o^2+2\right)-2\left(y_o^2-1\right)^4}{b_z^3\left(y_o^2+1\right)^8}, \tag{19}$$

$$\beta_2 = \frac{2b_z^2\left(y_o^2+1\right)^2\left(3y_o^6-20y_o^4+23y_o^2-2\right)-2\left(y_o^2-1\right)^4}{b_z^3\left(y_o^2+1\right)^8}.$$

For each (positive) value of $\mathcal{H}_0$, the possible trajectories of the Hamiltonian system defined by (18) belong to a family of ellipses with semimajor and semiminor axes $a$ and $b$ respectively. Thus, $\mathcal{H}_0 = \omega^2(a^2+b^2)/2$, and the angular momentum $G = xp_y - yp_x$ is expressed as $G = a\ b\ \omega$. Some of these ellipses become rectilinear orbits when $G = 0$. When $\mathcal{H}_1$ is taken into account, the system behaves as a perturbed harmonic oscillator and the trajectories can be described as ellipses whose orbital parameters evolve under the influence of the perturbation defined by $\mathcal{H}_1$. In this way, a normalization procedure allows us to reduce the problem to an integrable one-degree of freedom dynamical system [33].

For the normalization process, we follow the same scheme given in [34–36], which is accomplished as follows. In a first step, we express the Hamiltonian in Lissajous variables $(l, g, L, G)$ by means of the Lissajous transformation (see [37])

$$\mathcal{M} : (l, g, L, G) \longrightarrow (x, y, p_x, p_y),$$

defined in the domain

$$D = \{0 \le l < 2\pi\} \times \{0 \le g < 2\pi\} \times \{L > 0\} \times \{|G| \le L\},$$

by the equations

$$\begin{aligned} x &= s\cos(g+l) - d\cos(g-l), \\ y &= s\sin(g+l) + d\sin(g-l), \\ p_x &= -\omega[s\sin(g+l) + d\sin(g-l)], \\ p_y &= \omega[s\cos(g+l) + d\cos(g-l)], \end{aligned} \tag{20}$$

where $\omega s^2 = (L+G)/2$ and $\omega d^2 = (L-G)/2$. In the Lissajous variables, the Hamiltonian

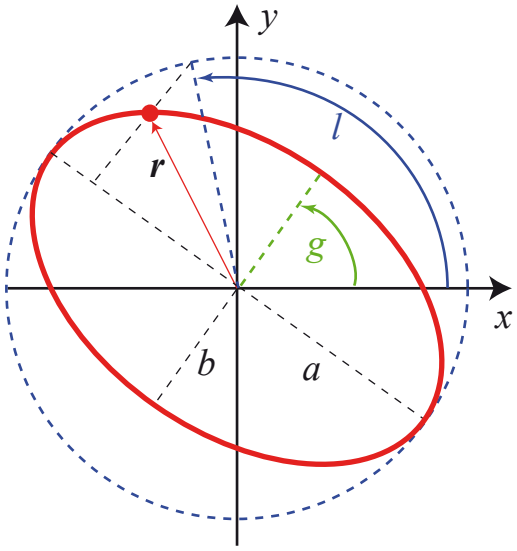


FIG. 6. Geometric meaning of the Lissajous angles $(l, g)$. Adaptation of Fig.1 in [37]. The red ellipse of semiaxes $a$ and $b$ is the unperturbed trajectory of the particle, while vector $\mathbf{r}$ stands for its instantaneous position on the ellipse.

$\mathcal{H} = b_z + \mathcal{H}_0 + \mathcal{H}_1$, up to polynomials of degree four, reads as

$$\mathcal{H}_0 = \omega L, \tag{21}$$

$$\mathcal{H}_1 = -\alpha \left(d^2 - 2ds\cos(2l) + s^2\right)\left(d\sin(g-l) - s\sin(g+l)\right) + \tag{22}$$

$$\left(d^2 - 2ds\cos(2l) + s^2\right)\left(\beta_1(d\cos(g-l) - s\cos(g+l))^2 + \right. \tag{23}$$

$$\left.\beta_2(d\sin(g-l) - s\sin(g+l))^2\right). \tag{24}$$

It is worth noting that this transformation is very convenient to handle elliptic oscillators, because $\mathcal{H}_0$ reduces to the simple form $\omega L$, being $L = (a^2+b^2)\omega/2$. The geometric meaning of the Lissajous angles $(l, g)$ is depicted in Fig.6. In particular, $l$ is a fast angular variable that reckons the motion along the ellipses, and we can assume that the perturbation causes a distortion in the elliptic orbits, in such a way that their size and orientation slowly change through the variables $(L, g, G)$. Thus, the angle $l$, the so-called elliptic anomaly, can be eliminated by means of an averaging process. After that, the problem gets reduced to a one-degree of freedom integrable dynamical system, where the new Hamiltonian admits the action $L$ as a new formal integral. We carry out this reduction by means of a Lie

transformation [38] up to order 2, so that the normalized Hamiltonian $\mathcal{K}$ is given by

$$\mathcal{K} = b_z + \mathcal{K}_0 + \mathcal{K}_1 = b_z + \omega L - \frac{25\alpha^2 L^2}{12\omega^4} + \frac{3L^2(\beta_1+\beta_2)}{4\omega^2} + \frac{(\alpha^2 - \omega^2(\beta_1+\beta_2))}{4\omega^4} G^2$$

$$- \frac{L^2\left(20\alpha^2 + 9\omega^2(\beta_1-\beta_2)\right)}{12\omega^4} e\cos 2g, \tag{25}$$

where $e = \sqrt{1 - G^2/L^2}$, $\mathcal{K}_0 = \mathcal{H}_0 = \omega L$ and $\mathcal{K}_1$ stands for the second order truncated normalized Hamiltonian, which is obtained from the Taylor series expansion up to fourth degree. Because $\mathcal{K}$ corresponds to a one-degree of freedom system, the contour lines of $\mathcal{K}$ onto the plane (actually the cylinder) $(g, G)$ are the phase trajectories of the normalized system. However, this representation on the cylinder $(g, G)$ does not cover the entire phase space, because the angle $g$ is not defined for the case of the circular orbits, that appears when $|G| = L$. This singularity is overcome [35, 39] when the system is expressed in the Hopf variables

$$\xi_1 = e\cos 2g, \quad \xi_2 = e\sin 2g, \quad \xi_3 = \frac{G}{L}. \tag{26}$$

It is easy to check that $\xi_1^2 + \xi_2^2 + \xi_3^2 = 1$ and the phase space consists of a unit radius sphere. In these coordinates, the points such that $\xi_3 > 0$ $(G > 0)$ stand for ellipses traveled in a prograde sense, while if $\xi_3 < 0$ $(G < 0)$ the ellipses are traveled in a retrograde sense. Furthermore, any point on the equatorial circle $\xi_3 = 0$ $(G = 0)$ corresponds to a rectilinear orbit passing through the origin. Finally, the north (south) pole corresponds to circular orbits $(e = 0)$ traveled in direct (retrograde) sense.

In the Hopf variables $(\xi_1, \xi_2, \xi_3)$, Hamiltonian (25) can be written in this simple form:

$$\mathcal{K} = a_1\xi_1 + a_2\xi_3^2, \tag{27}$$

where the coefficients $a_1$ and $a_2$ are given by

$$a_1 = -\frac{L^2\left(20\alpha^2 + 9\omega^2(\beta_1-\beta_2)\right)}{12\omega^4} = \frac{L^2\left(y_o^6 + 3y_o^4 + 27y_o^2 + 9\right)}{6\left(y_o^4 - 1\right)^2}, \tag{28}$$

$$a_2 = \frac{L^2\left(\alpha^2 - \omega^2(\beta_1+\beta_2)\right)}{4\omega^4} = \frac{L^2\left(y_o^2 - 1\right)^2}{4b_z^2\left(y_o^2 + 1\right)^4}, \tag{29}$$

being $a_1 < 0$ and $a_2 > 0$, and where the constant terms appearing in (25) have been dropped. It is worth noticing that (27) belongs to the so-called Quadratic Hamiltonian family which has been extensively studied by Lanchares and Elipe [40–42]. Taking into account the Poisson brackets between the variables $(\xi_1, \xi_2, \xi_3)$,

$$[\xi_1, \xi_2] = \xi_3, \quad [\xi_2, \xi_3] = \xi_1, \quad [\xi_3, \xi_1] = \xi_2,$$

the Hamiltonian equations of motion arising from (27) are

$$\begin{aligned}\dot{\xi}_1 &= [\xi_1, \mathcal{K}] = -2a_2\xi_2\xi_3,\\ \dot{\xi}_2 &= [\xi_2, \mathcal{K}] = (2a_2\ \xi_1 - a_1)\xi_3,\\ \dot{\xi}_3 &= [\xi_3, \mathcal{K}] = a_1\xi_2.\end{aligned} \tag{30}$$

The equilibria of the reduced system are the solutions of the system of equations formed by (30) equated to zero. It is straightforward to see that there are just the four following isolated equilibria:

$$\epsilon_{1,2} = (\pm 1, 0, 0), \quad \epsilon_{3,4} = (a_1/2a_2, 0, \pm\sqrt{1-(a_1/2a_2)^2}). \tag{31}$$

The equilibrium $\epsilon_1 = (1, 0, 0)$ corresponds to rectilinear orbits (i.e., orbits with $G = 0$) along the $y$ axis, whereas the equilibrium $\epsilon_2 = (-1, 0, 0)$ corresponds to rectilinear orbits along the $x$ axis. We note that, in the $(g, G/L)$ variables, each equilibrium unfolds into the two points: $(0, 0)$ and $(\pi, 0)$ for $\epsilon_1$; $(\pi/2, 0)$ and $(3\pi/2, 0)$ for $\epsilon_2$. Because the quotient $a_1/(2a_2)$ is always negative, the equilibria $\epsilon_{3,4}$ correspond to elliptical orbits with $g = \pi/2$ and $g = 3\pi/2$ traveled in direct and retrograde senses, respectively. Because the phase space trajectories are living on the unit sphere, the equilibria $\epsilon_{3,4}$ only exist when $|a_1|/(2a_2) \leq 1$. When $|a_1|/(2a_2)$ passes through the value 1, a bifurcation is expected and from that bifurcation only the equilibria $\epsilon_{1,2}$ will survive. See [40–42] for more information about bifurcations in biparametric quadratic Hamiltonians.

The critical value $|a_1|/(2a_2)$ defines a curve that divides the parameter plane $(b_x, b_z)$ into different regions, where the number of equilibrium points changes. Using the expressions (28) and (29), for $a_1$ and $a_2$, the bifurcations curves are:

$$\gamma_1 \equiv -3b_x^6 + b_x^4\left(4b_z^2+6\right) + b_x^2\left(4\left(\sqrt{1-b_x^2}+1\right)b_z^2 - 3\right) - 2\left(\sqrt{1-b_x^2}-1\right)b_z^2 = 0, \tag{32}$$

$$\gamma_2 \equiv 2\left(2\left(b_x^2 - \sqrt{1-b_x^2}+1\right)b_x^2 + \sqrt{1-b_x^2}+1\right)b_z^2 - 3b_x^2\left(b_x^2-1\right)^2 = 0, \tag{33}$$

where $\gamma_1$ (the red curve in Fig.7) is the bifurcation curve for the inner potential well, when $y_o = y_1 = (1-\sqrt{1-b_x^2})/b_x$, whereas $\gamma_2$ (the blue dashed curve in Fig.7) is the bifurcation curve for the outer potential well, when $y_o = y_4 = (1+\sqrt{1-b_x^2})/b_x$. It follows that, below the curves $\gamma_{1,2}$ ($|a_1|/(2a_2) < 1$) the number of equilibria is four ($\epsilon_{1,2,3,4}$) and, when $\gamma_{1,2}$ are crossed, above those curves ($|a_1|/(2a_2) > 1$) the number of equilibria changes to two ($\epsilon_{1,2}$).

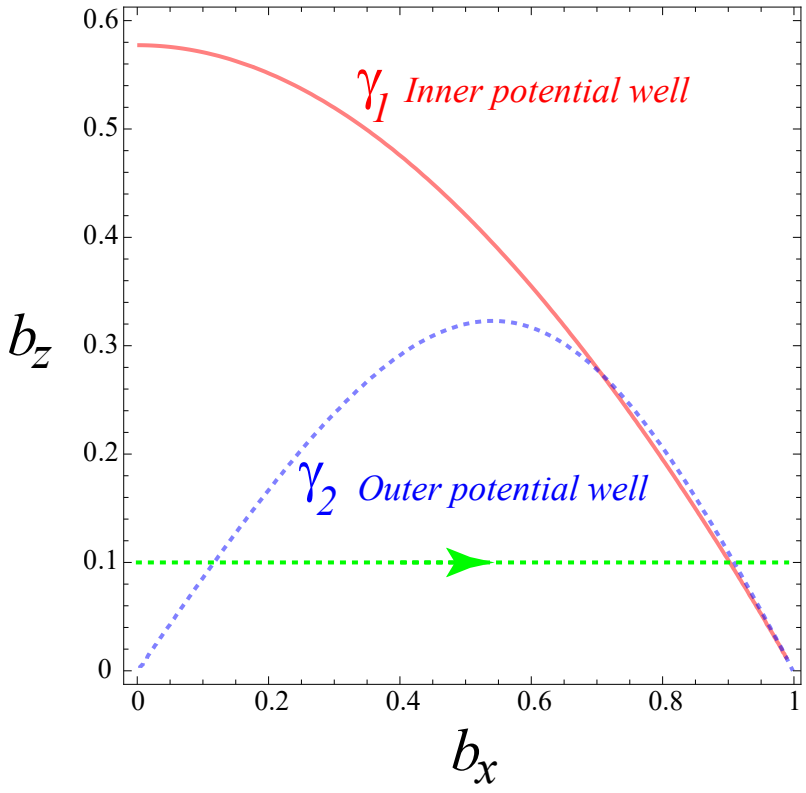


FIG. 7. Bifurcations curves $|a_1|/(2a_2) = 1$ in the $(b_x, b_z)$ plane for the inner (red curve $\gamma_1$) and for the outer (blue dashed curve $\gamma_2$) potential wells that appear when $b_x \leq 1$. The green dashed line indicates the path in the parameter plane $(b_x, b_z)$ used for the investigation of the phase flow.

From the shape and the expression (32) of the bifurcation curve $\gamma_1$, we find that just one bifurcation is possible when $b_z < 1/\sqrt{3}$. Above the value $b_z = 1/\sqrt{3}$, the number of equilibria is always two ($\epsilon_{1,2}$). However, from the shape and the expression (33) of $\gamma_2$, we obtain that, for $b_z \lesssim 0.322991$, two bifurcations may occur, when $b_x$ varies from 0 to 1, while, above that value, bifurcations are not possible and the number of equilibria is always two ($\epsilon_{1,2}$). Finally, a simultaneous bifurcation takes place in both potential wells when $\gamma_1$ and $\gamma_2$ are crossed at the common intersection point $b_x = 1/\sqrt{2}$ and $b_z = \sqrt{3/40}$.

We perform the linear stability analysis of the equilibria by studying the roots of the characteristic equation resulting from the variational equations of motion [43, 44]. After some calculations, we find that the characteristic equation is given by

$$4a_1a_2^2\xi_2\xi_3 - (2a_1a_2\xi_1 - a_1^2 - 4a_2^2\xi_3^2)\lambda + \lambda^2 = 0. \tag{34}$$

By substituiting in (34) the coordinates of the equilibria (31), we obtain the following sta-

bility properties:

- $\epsilon_1$ is always stable because the roots of its characteristic equation,

$$\lambda^2 + 2|a_1|a_2 + a_1^2 = 0,$$

  are always imaginary.

- The characteristic equation for $\epsilon_2$ is

$$\lambda^2 - (2|a_1|a_2 - a_1^2) = 0.$$

  On the one hand, when $|a_1|/(2a_2) < 1$ (i.e., below the $\gamma_{1,2}$ curves), the roots $\lambda$ are real, so that $\epsilon_2$ is unstable. On the other hand, when $|a_1|/(2a_2) > 1$ (above the $\gamma_{1,2}$ curves), they are imaginary, and $\epsilon_2$ is stable.

- The characteristic equation for $\epsilon_{3,4}$ is

$$\lambda^2 - (a_1^2 - 4a_2^2) = 0.$$

  Because these equilibria only exist when $|a_1|/(2a_2) < 1$ (below the $\gamma_{1,2}$ curves), the roots corresponding to $\epsilon_{3,4}$ are always imaginary, and, when they exist, they are stable.

The stability analysis confirms again that when the $\gamma_{1,2}$ curves are crossed (i.e., when $|a_1|/(2a_2) = 1$) a bifurcation occurs. The existence of this bifurcation can also be detected by studying the evolution of the energy of the equilibria. The energies of the equilibria are respectively,

$$\mathcal{K}_1 = -|a_1|, \quad \mathcal{K}_2 = |a_1|, \quad \mathcal{K}_{3,4} = \frac{a_1^2 + 4a_2^2}{4a_2}.$$

The energy $\mathcal{K}_1$ of $\epsilon_1$ is the minimum energy of the system and, as a consequence of Lyapunov Theorem [45], $\epsilon_1$ is always stable. When $|a_1|/(2a_2) < 1$, the energy reaches its absolute maximum at the equilibria $\epsilon_{3,4}$ with value $\mathcal{K}_{3,4}$. Again, by virtue of Lyapunov Theorem, these equilibria are stable. As $|a_1|/(2a_2)$ approaches the critical value, the energy $\mathcal{K}_{3,4}$ of $\epsilon_{3,4}$ tends to the energy $\mathcal{K}_2$ of $\epsilon_2$, so that at $|a_1|/(2a_2) = 1$, $\mathcal{K}_{3,4} = \mathcal{K}_2$ and $\epsilon_{3,4}$ disappear. Then, when $|a_1|/(2a_2) > 1$, $\mathcal{K}_2$ becomes the absolute maximum of the energy and for that reason $\epsilon_2$ becomes stable.

A more detailed visualization of the normalized dynamics provided by the Hamiltonian $\mathcal{K}$ is obtained from the phase flow evolution as a function of the parameters $a_1$ and $a_2$. To

carry out this study, we fix the value of the bias field $b_z = 0.1$ and we vary the value of the field $b_x$. In other words, we follow the straight path in the parameter plane $(b_x, b_z)$ depicted by the green dashed line in Fig.7.

In the inner potential well around the minimum $P_1 = (0, (1 - \sqrt{1 - b_x^2})/b_x)$, the bifurcation curve $\gamma_1 \equiv |a_1|/(2a_2) = 1$ is crossed for $b_z = 0.1$ at the critical value $b_x \approx 0.9022$. In Figure 8 the phase flow evolution on the Hopf sphere corresponding to Hamiltonian (27) for five values of $b_x$ along the straight path $b_z = 0.1$ is shown. When $b_x$ is far below the critical value $b_x \approx 0.9022$ (see the first and second rows in Fig. 8 for $b_x = 0.1$ and $b_x = 0.5$), the stable equilibria $\epsilon_{3,4}$ appear close to the north and south poles respectively, and the separatrix passing through $\epsilon_2 = (-1, 0, 0)$ establishes two regions of motion. On the one side, the levels around the stable equilibrium $\epsilon_1 = (1, 0, 0)$, which correspond to quasiperiodic orbits with the same symmetry pattern as $\epsilon_1$, i.e., mainly aligned along the $y$ axis. On the other side, the levels around $\epsilon_{3,4}$, which correspond to quasiperiodic trajectories around the elliptic orbits $\epsilon_{3,4}$. Examples of these two kinds of orbits are shown in Fig.9 for $b_x = b_z = 0.1$ and energy $E = 0.12$. These orbits are represented in the $x$-$y$ plane and they have been obtained from the numerical integration of the equations of motion (30) associated to the normalized Hamiltonian $\mathcal{K}$ given by Eq.(27). Then, transformations (26) and (20) were applied. As $b_x$ approaches the critical value $b_x \approx 0.9022$ (see the third and fourth rows in Fig. 8 for $b_x = 0.85$ and $b_x = 0.89$) the equilibria $\epsilon_{3,4}$ approach the equilibrium $\epsilon_2$. As a consequence, the phase space region of trajectories around $\epsilon_{3,4}$ shrinks, and at the critical value $b_x \approx 0.9022$, a pitchfork bifurcation occurs: The three equilibria collide, and from this bifurcation only the equilibrium $\epsilon_2$ survives, becoming stable. Then, for $b_x > 0.9022$ (see the fifth row in Figure 8 for $b_x = 0.92$), the phase flow is made of levels around $\epsilon_1$ and $\epsilon_2$. In other words, after the bifurcation only trajectories around the rectilinear orbits $\epsilon_{1,2}$ exist: The nearer an orbit is to $\epsilon_1$ ($\epsilon_2$), the greater its orientation is along the $y$ ($x$) axis.

In the outer potential well, the coordinate of the corresponding minimum is $P_4 = (0, (1 + \sqrt{1 - b_x^2})/b_x)$, and for $b_z = 0.1$ the critical values of $b_x$ take place when the bifurcation curve $\gamma_2 \equiv |a_1|/2a_2 = 1$ is crossed at $b_x \approx 0.1169$ and at $b_x \approx 0.9089$. We note that $\gamma_2$ takes a maximum value at $b_x \approx 0.5410$ and $b_z \approx 0.322991$, so that, above this maximum the number of equilibria is always two. Thence, we expect two bifurcations and different dynamics in the three regions defined by the intervals $0 \leq b_x \lesssim 0.1169$, $0.1169 \lesssim b_x \lesssim 0.9089$

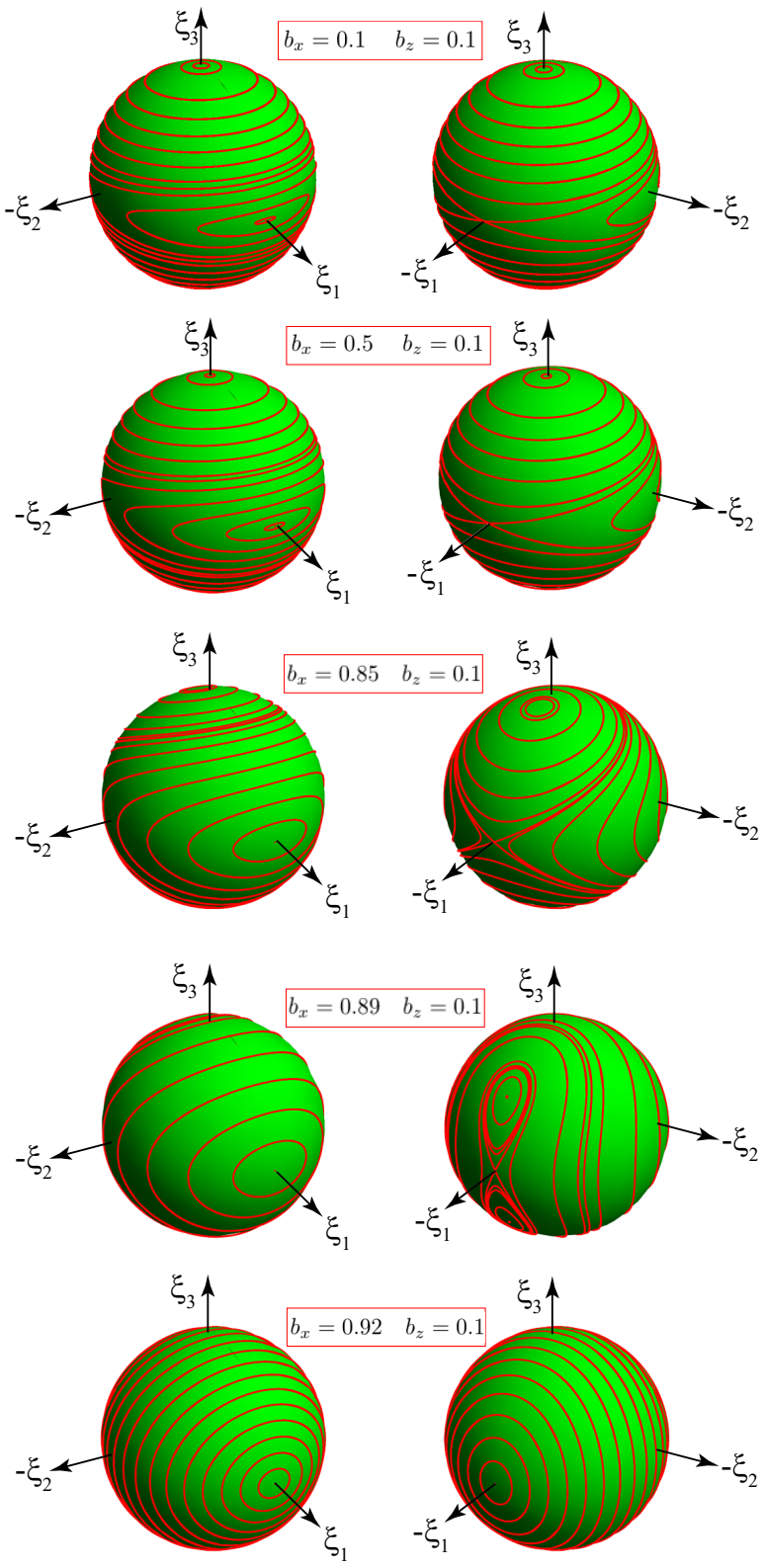


FIG. 8. Phase flow evolution of the normalized system corresponding to the dynamics in the inner potential well.

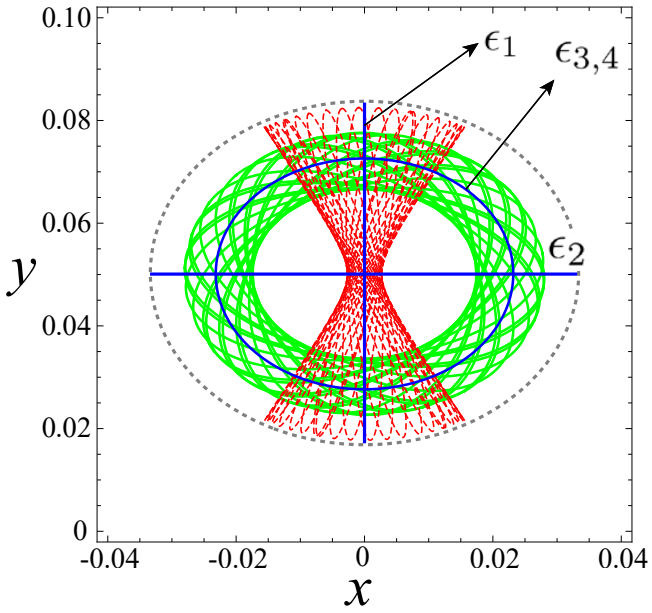


FIG. 9. The blue lines are the periodic orbits corresponding to the equilibrium points $\epsilon_{1,2,3,4}$. The red and the green orbits are characteristic orbits around the equilibrium points $\epsilon_1$ and $\epsilon_{3,4}$, respectively. All trajectories have been calculated for $b_x = b_z = 0.1$ and energy $E = 0.12$, and they were obtained from the numerical integration of the equations of motion (30) arising from the normalized Hamiltonian $\mathcal{K}$ given by Eq.(27). The black dotted curve is the equipotential curve $E = 0.12 = V(x, y)$.

and $0.9089 \lesssim b_x < 1$ (see Fig.7). The phase flow evolution corresponding to Hamiltonian (27) across these three regions, is depicted in Figure 10 for $b_z = 0.1$. In the first row of Fig.10, for $b_x = 0.1$, the phase flow is made of trajectories around the stable equilibria $\epsilon_{1,2}$. At $b_x \approx 0.1169$ a pitchfork bifurcation occurs and from $\epsilon_2$, which becomes unstable, the stable equilibria $\epsilon_{3,4}$ are born (see the second row of Fig.10 for $b_x = 0.15$). As $b_x$ increases in the interval $0.1169 \lesssim b_x \lesssim 0.5410$, the equilibria $\epsilon_{3,4}$ move towards the north and south poles and the phase space around them grows (see the third row of Fig.10 for $b_x = 0.25$). Then, when $b_x$ increases in the interval $0.5410 \lesssim b_x \lesssim 0.9089$, the equilibria $\epsilon_{3,4}$ describe the reverse way (see the fourth row of Fig.10 for $b_x = 0.9$) so that, at $b_x \approx 0.9089$ they collide with $\epsilon_2$ and a second pitchfork bifurcation takes place. From this bifurcation, only $\epsilon_2$ survives, becoming stable. In the interval $0.9089 \lesssim b_x < 1$ we recover the same phase flow structure as in the first region (see the fifth row of Fig.10 for $b_x = 0.92$). As in the previous case where the normalized phase flow was studied in the inner potential well, in all cases

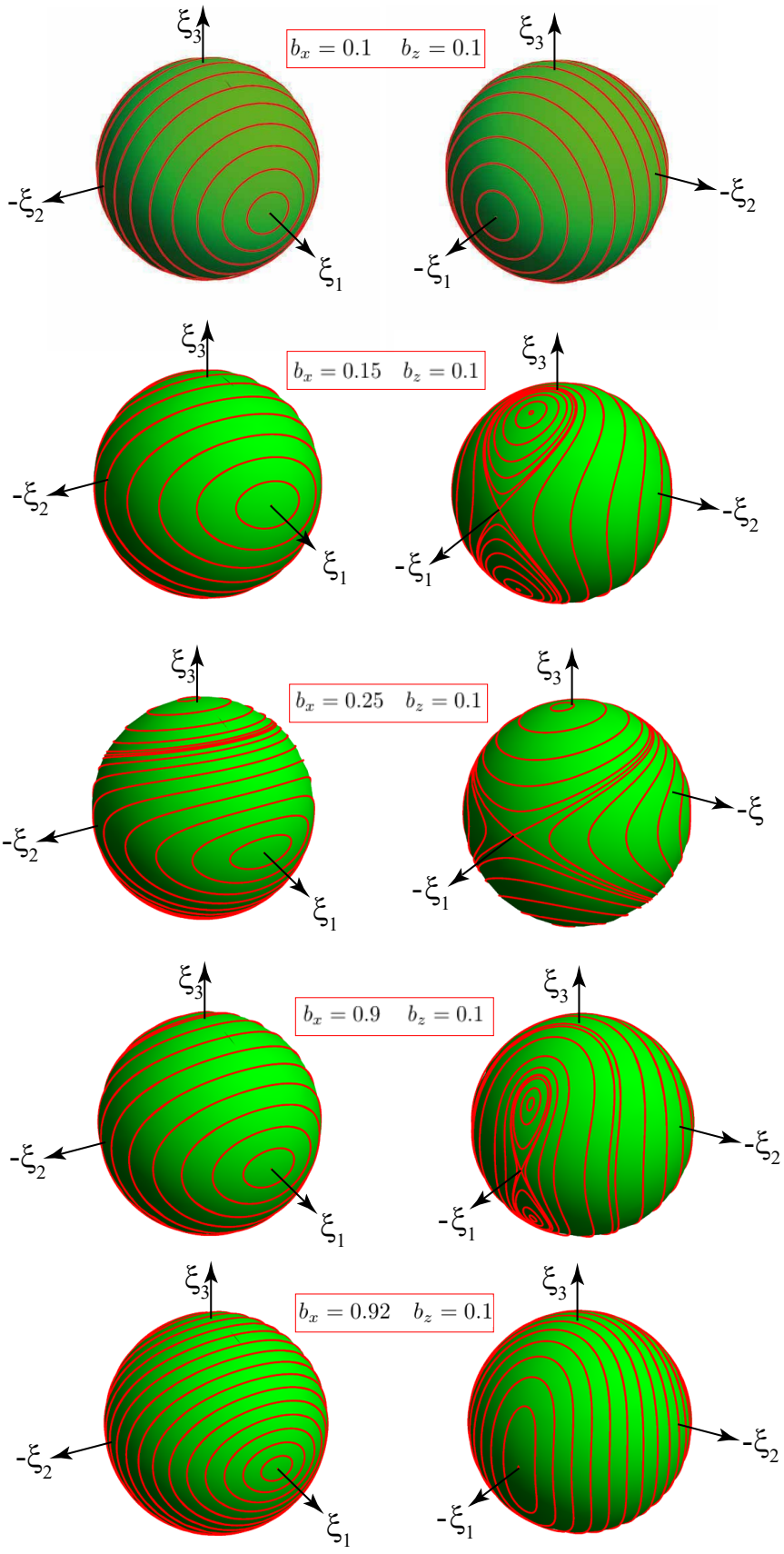


FIG. 10. Phase flow evolution of the of the normalized system corresponding to the dynamics in the outer potential well.

the symmetry pattern of a given trajectory is determined by the nature of the equilibrium point (periodic orbit) around which such a trajectory is living.

The normalized Hamiltonian (27) is expected to be useful in describing the dynamics when the energy of the system is close enough to the energy $E_{1,4} = b_z$ of the minima $P_{1,4}$, i.e. close to its integrable limit. Therefore, a comparison between the phase flow of the reduced system and the phase flow of the original one would be appropriate and it will be carried on in the next section.

### C. Phase Flow Structure

In this subsection we focus on the structure and evolution of the phase flow as a function of the parameters of the system, namely $b_x$, $b_z$ and the energy $E$. Because the system at hand has two degrees of freedom, the Poincaré sections are the most convenient tool for this purpose.

To begin with, we fix $b_z = 0.1$ and also the energy of the system, $E = 0.12$, close enough to the energy of the critical points $P_{1,4}$, and vary $b_x$ from 0 to 1, that is to say, we follow again the straight path in the parameter plane $(b_x, b_z)$ depicted by the green dashed line in Fig.7. In this way, both bifurcations curves $\gamma_{1,2}$ are crossed for increasing values of $b_x$, and most of the possible relevant dynamical situations described in Subsec. IV B are expected to be found.

A convenient Poincaré map is $p_x = 0$ with $\dot{p}_x \geq 0$, so that the sections appear in the plane $(y, p_y)$. Under these conditions, the available region of the surfaces of section is limited by the curves

$$p_y = \pm \sqrt{2\left(E - \sqrt{\left(b_x - \frac{2y}{y^2+1}\right)^2 + b_z^2}\right)}. \tag{35}$$

It is worth noting that rectilinear orbits $I_y$ are tangent to the flux in this Poincaré map, and they correspond to the curves (35). For values of the energy below the saddle point energy $E_2 = \sqrt{(1-b_x)^2 + b_z^2}$, the Poincaré sections are made of two disjoint regions encircling the two minima $P_1$ and $P_4$. For $b_z = 0.1$, the energy of the minima $P_{1,4}$ is $E_{1,4} = b_z = 0.1$ and, if the total energy $E$ of the system is close to that energy, the dynamics is expected to be near integrable. This situation is depicted in Fig.11, where the Poincaré sections for $E = 0.12$, $b_z = 0.1$ and $b_x = 0.1$, $b_x = 0.5$, $b_x = 0.85$ and $b_x = 0.92$ are shown. The left and right

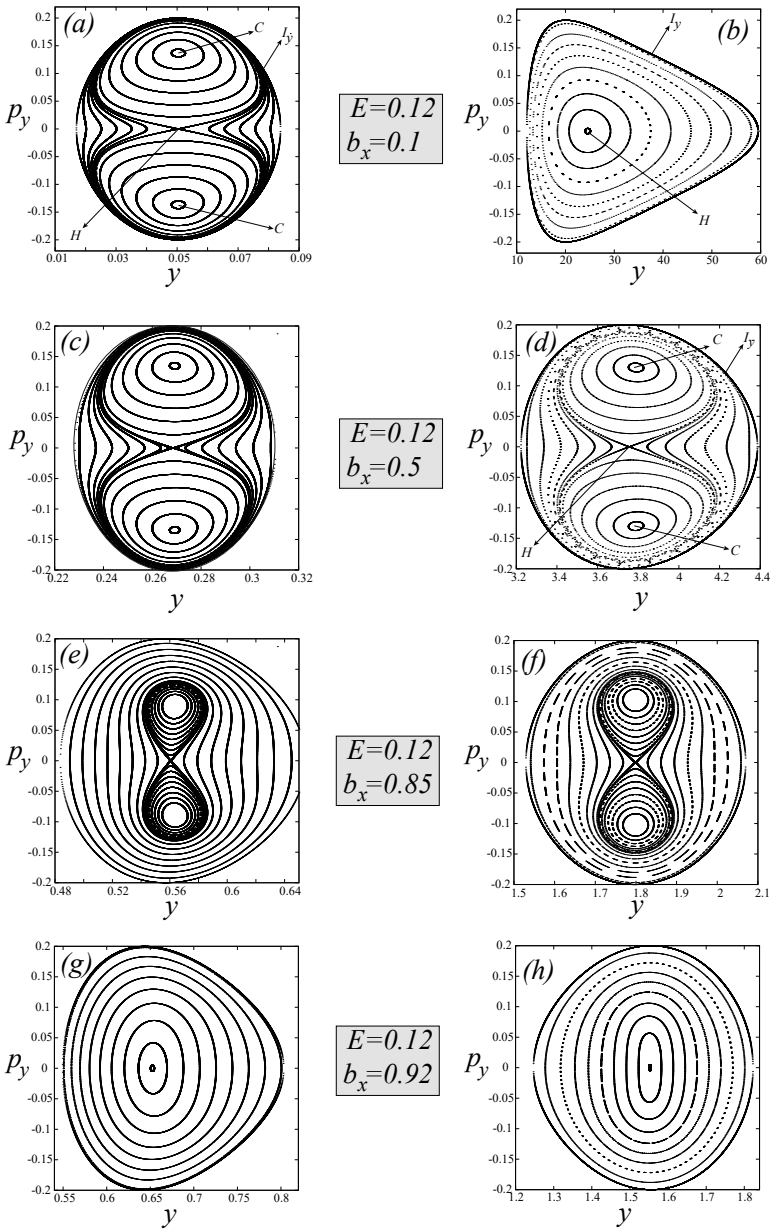


FIG. 11. Poincaré sections $p_x = 0$ with $\dot{p}_x \geq 0$ for $b_x = 0.1$, $b_x = 0.5$, $b_x = 0.85$ and $b_x = 0.92$, and for the energy $E = 0.12$ and $b_z = 0.1$. Because the energy $E = 0.12$ is in all cases below the saddle point energy $E_2 = \sqrt{(1 - b_x)^2 + b_z^2}$, the Poincaré sections are made of two disjoint regions shown in the left and in the right panels, respectively.

hand panels of Fig.11 correspond to the surfaces of section around the minimum $P_1$ and $P_4$, respectively.

For $b_z = 0.1$ and $b_x = 0.1$, the system is below the bifurcation curve $\gamma_1$ and above the bifurcation curve $\gamma_2$ (see Fig.7), and the corresponding surface of section (Fig.11(a)-(b))

indicates that the phase flow shows different structure around the minimum $P_1$ than around the minimum $P_4$. From Fig.11(a), the surface of section around the minimum $P_1$, we account for the following well defined structures:

i) Two stable fixed points symmetrically located above and below the $y$ axis, named $C$, corresponding to almost circular orbits traveled in opposite directions. The levels around these points are quasiperiodic orbits with the same symmetry patterns as $C$. For the energy $E = 0.12$, in Fig.12(a), the periodic orbit $C$ and a representative quasiperiodic orbit around it are shown.

ii) A homoclinic orbit (separatrix) passing through the hyperbolic (unstable) fixed point located at the $p_y = 0$ axis, which separates the motion around the orbits $C$. We name this point as $H$ and corresponds to an almost rectilinear orbit parallel to the $x$ axis. For $E = 0.12$, the periodic orbit $H$ is depicted in Fig.12(a).

iii) Finally, taking into account that the limit of the surface of section is the rectilinear orbit $I_y$, the levels above the separatrix passing through $H$ are quasiperiodic orbits mainly oriented along the $y$ axis. The periodic orbit $I_y$ and a representative quasiperiodic orbit around it are shown in Fig.12(a). While the stability of $C$ and $H$ can be established at a glance, the stability of $I_y$ (i.e., the limit of the Poincaré map) must be determined by using the Index Theorem. Indeed, because the domain $D$ of the surface of section is homeomorphic to a two-dimensional sphere, the sum of the indexes of the fixed points is 2. Because Fig.11(a) shows one unstable critical point (with index -1) and two stable fixed points (with index 1), the index of the periodic orbit $I_y$ must be 1 in order to keep fixed the Euler characteristic to 2. Then, $I_y$ is a stable periodic orbit.

However, in the surface of section of Fig.11(b) around the minimum $P_4$ there is just a single stable fixed point (periodic orbit). We also name $H$ this periodic orbit, because it corresponds to an arch-like orbit oriented along the $x$ axis. Due to the fact that the limit of the surface of section in Fig.11(b) is the rectilinear orbit $I_y$, this periodic orbit, $I_y$, is stable because the Euler characteristic of the surface of section must be 2. The circulations around $H$ indicate that the phase space is made of quasiperiodic orbits that show a smooth evolution in their orientation: The nearer a circulation is to $H$ ($I_y$), the greater the orientation of the corresponding quasiperiodic orbits is along $H$ ($I_y$). In Fig.12(b) the periodic orbits $H$ and $C$ and two representative quasiperiodic orbits are depicted.

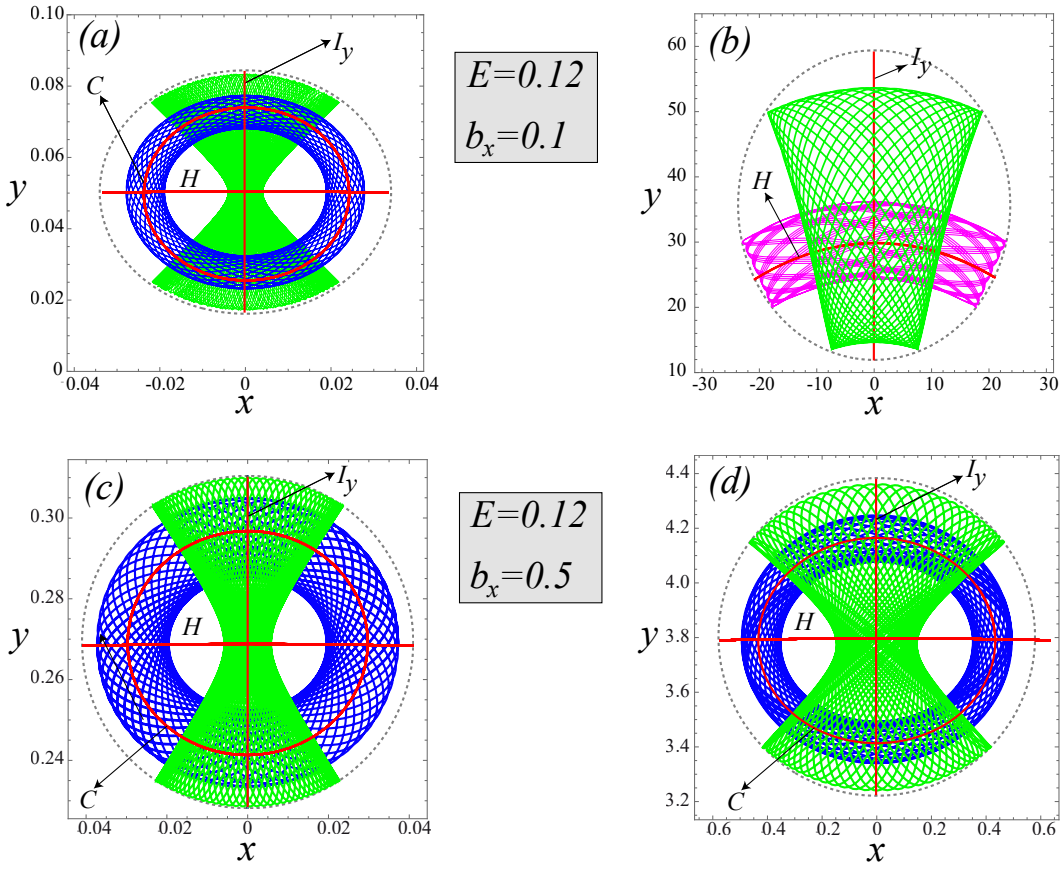


FIG. 12. Periodic orbits $C$ (stable), $H$ (unstable) and $I_y$ (stable) appearing in the surfaces of section of Fig.11(a)-(c) (left panels) and Fig.11-(b)-(d) (right panels). The blue, green and pink orbits are representative quasiperiodic orbits around $C$, $I_y$ and $H$, respectively. The black dotted lines are the corresponding equipotential curves $E = V(x, y) = 0.12$. All figures are made for $b_z = 0.1$ and $E = 0.12$.

For $b_x = 0.5$ and $b_z = 0.1$, the system is below both $\gamma_{1,2}$. As we observe in the surface of section in Fig.11(c)-(d), while the structure of the phase flow is qualitatively the same around $P_1$, the phase flow structure around $P_4$ has changed. Indeed, Fig.11(d) shows that the unstable fixed point $H$ becomes unstable and a separatrix passing through it encloses two stable fixed points denoted by $C$. In other words, the periodic orbit $H$ living in the outer potential well experiences a pitchfork bifurcation. In Fig.12(c)-(d), the periodic orbits $H$, $C$ and $I_y$, as well as representative quasiperiodic orbits around them, are shown.

When the value of $b_x$ increases below the bifurcation curves $\gamma_{1,2}$ (i.e., for $b_x$ below the critical values $b_x \approx 0.9022$ and $b_x \approx 0.9089$ for $\gamma_1$ and $\gamma_2$ respectively, for $b_z = 0.1$), although

the structure of the phase flow remains qualitatively unchanged (see Fig.11(e)-(f) for $b_x = 0.85$), we observe that the fixed points $C$ approach the unstable fixed point $H$. Then, the size of the phase space region with $C$-shaped quasiperiodic orbits shrinks, while the phase space region above the separatrix grows in size. Finally, when both $\gamma_{1,2}$ are crossed, at the above critical values of $b_x$, the stable fixed points $C$ collapse into $H$, which becomes stable (see the Poincaré map for $b_x = 0.92$ of Fig.11(g)-(h)). That is to say, two consecutive pitchfork bifurcations between the stable periodic orbits $C$ and the unstable periodic orbit $H$, living, respectively, around $P_1$ and $P_4$, take place, so that, from these bifurcations, only the corresponding periodic orbit $H$ survives, becoming stable.

When we compare the left and the right panels in Fig.11, we observe that tight trapping is in general attained in the phase space region around the minimum $P_1$ because the size of the inner phase space region is always smaller than the size of the phase space in the outer region. Furthermore, the smaller the value of $b_x$ is, the larger the size difference. This fact is related with the frequency ratio $\eta = \omega_1/\omega_4$ between the harmonic frequencies around the inner and the outer potential wells (see Fig.5). Indeed, the fast increase of $\eta$, for decreasing values of $b_x$, indicates that the width of the outer potential well grows very fast, almost exponentially.

It is worth noticing the good agreement between the structure of the phase flow predicted by perturbation methods (see Fig.8 and Fig.10) and the real structure shown in the Poincaré maps of Fig.11. In this way, the equilibrium points $\epsilon_1$, $\epsilon_2$ and $\epsilon_{3,4}$ in the reduced dynamics correspond, respectively, to the periodic orbits $I_y$, $H$ and $C$ that occur in the Poincaré sections of Fig.11. Furthermore, the examples of orbits obtained using the Lissajous normal form that are depicted in Fig.9 show the same pattern as the examples of quasiperiodic orbits presented in Fig.12(a). In fact, this is a consequence of Reeb's Theorem, which ensures the matching between non degenerate critical points of the averaged system and periodic orbits of the original one, if the energy is close enough to $E_{1,4}$ [46].

Now, we study the evolution of the phase flow as a function of the energy of the system. Then, we fix the values $b_x = 0.5$ and $b_z = 0.1$, and we vary the energy $E$. Because the energy of the saddle point $P_2$ is $E_2 = \sqrt{(1-b_x)^2 + b_z^2} \approx 0.5385$, the motion is still confined within either of the potential wells around the minima $P_1$ or $P_4$, whenever $E < E_2$. For $E = 0.2$, the corresponding twofold Poincaré section is shown in Fig.13. It is observed again

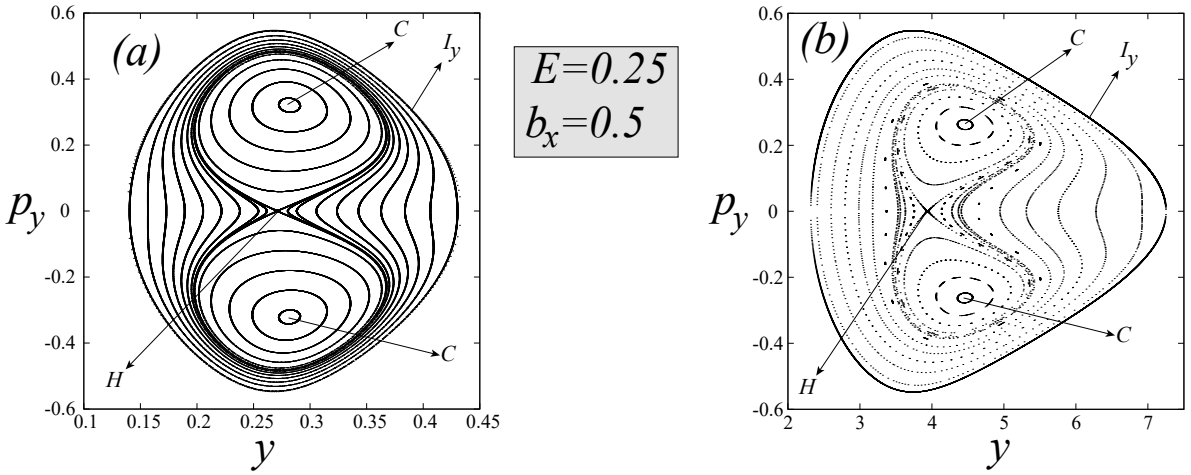


FIG. 13. Poincaré section $p_x = 0$ with $\dot{p}_x \geq 0$ for $b_x = 0.5$, $b_z = 0.1$ and for the energy $E = 0.25$. Because the energy $E = 0.25$ is below the saddle point energy $E_2 \approx 0.5099$, the Poincaré section is made of two disjointed regions shown in the left and in the right panels.

the difference between the phase space size around the inner and the outer potential wells, which can be explained by the large value of the frequency ratio $\eta = \omega_1/\omega_4 \approx 13.9282$ for $b_x = 0.5$, that confirms the tight trapping around the minimum $P_1$. Closely related to this issue, but not apparent in the Poincaré section of Fig.13 nor in the sections of Fig.11, are the time scales of the dynamics, depending on whether a given orbit is living in the inner or in the outer potential well. A first glimpse can be obtained from the periods $\tau_C$, $\tau_{I_y}$ and $\tau_H$ of the periodic orbits $C$, $I_y$ and $H$, appearing in Fig.13. Indeed, in Table II, we observe that the dynamics is rather slow in the outer region of the phase space located around the minimum $P_4$ than in the region around the inner minimum $P_1$. Furthermore, the ratios $\eta_C$, $\eta_{I_y}$ and $\eta_H$ between the periods of $C$, $I_y$ and $H$ in the outer and in the inner potential wells (see the third row of Table II) are, in particular for $I_y$ and $H$, very close to the value 13.9282 predicted by the frequency ratio $\eta$ for $b_x = 0.5$.

For $E = 0.5$, an energy close enough but below the saddle energy $E_2 \approx 0.5385$, the Poincaré map is still made of two disjoint regions. However, the dynamics is different in each region. While in the outer region, represented in Fig.14(b), the dynamics remains regular, in Fig.14(a) we observe that the inner region of the phase space underwent a drastic change in its structure. Indeed, the former separatrix passing through the hyperbolic orbit $H$ has been replaced by a stochastic layer. Inside this stochastic layer, a rather large region

| | | | |
|---|---|---|---|
| I.P.W. | $\tau_C = 0.9807$ | $\tau_{I_y} = 1.3108$ | $\tau_H = 1.3261$ |
| O.P.W. | $\tau_C = 18.3939$ | $\tau_{I_y} = 18.6078$ | $\tau_H = 18.6384$ |
| | $\eta_C = 18.7559$ | $\eta_{I_y} = 14.1958$ | $\eta_H = 14.0550$ |

Table II. Periods $\tau_C$,$\tau_{I_y}$ and $\tau_H$ of the periodic orbits $C$, $I_y$ and $H$ appearing in Fig.13 for $b_x = 0.5$, $b_z = 0.1$ and for the energy $E = 0.25$. The acronyms I.P.W. and O.P.W. stand for inner and outer potential wells, respectively. $\eta_C$, $\eta_{I_y}$ and $\eta_H$ are the ratios between the periods $\tau_C$, $\tau_{I_y}$ and $\tau_H$ in the outer and in the inner potential wells.

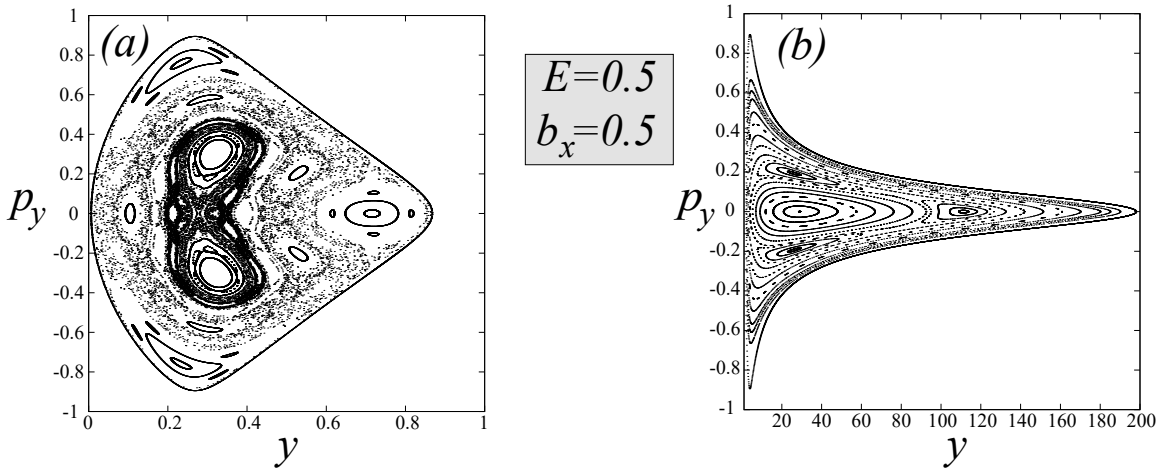


FIG. 14. Poincaré section $p_x = 0$ with $\dot{p}_x \geq 0$ for $b_x = 0.5$, $b_z = 0.1$ and for the energy $E = 0.5$. Although the energy $E = 0.5$ is close but still below the saddle point energy $E_2 \approx 0.5385$, the Poincaré section is made of two close but disjoint regions shown in the left and in the right panels, respectively.

of regular motion around the elliptic points $C$ persists. Outside the stochastic layer, there are many structures of regular islands that are embedded in a chaotic sea that fills large regions of the map. Note that the difference between the size of the inner and the outer phase space regions observed for small energy values is now much larger.

When $E$ is above the trap energy, $E_2 \approx 0.5385$, the surface of section is unbounded, and orbits may leave the trap. As we can observe in the surface of section for $E = 0.55$, shown in Fig.15, most of the orbits are unbounded and only the region around and inside the former separatrix passing through $H$, in the inner potential well, is able to keep bounded orbits.

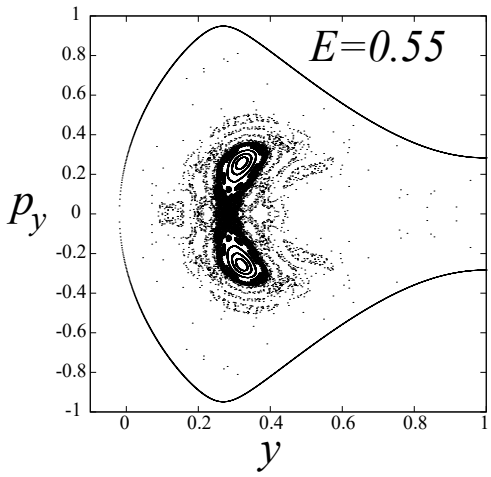


FIG. 15. Poincaré section $p_x = 0$ with $\dot{p}_x \geq 0$ for $b_x = 0.5$, $b_z = 0.1$ and for the energy $E = 0.55$. The energy $E = 0.55$ is slightly above the saddle point energy $E_2 \approx 0.5385$, and the Poincaré section is unbounded.

## V. DYNAMICS FOR THE CASE $b_x > 1$

### A. Classical perturbation theory

When $b_x > 1$, there are two potential wells centered on the critical points $P_{5,6}$, symmetrically located along the unit circle. Our goal is to study the dynamics in the vicinity of these points, as we did in the case $0 < b_x < 1$. The first step is to perform a translation in order to move the critical point to the origin. Thus, we introduce the canonical change of variables

$$x \to x' + x_o, \quad y \to y' + y_o, \quad p_x \to p'_x, \quad p_y \to p'_y$$

where

$$x_o = \pm\frac{\sqrt{b_x^2 - 1}}{b_x}, \quad y_o = \frac{1}{b_x},$$

are the coordinates of the minima $P_{5,6}$. Now, a Taylor series expansion around the origin, and after dropping primes, allows us to write the Hamiltonian as

$$\mathcal{H} = b_z + \frac{1}{2}(p_x^2 + p_y^2) + \frac{1}{2}\omega^2(x^2+y^2) + (\alpha_1 x + \alpha_2 y)(x^2+y^2) + (\beta_1 x^2 + \beta_2 xy + \beta_3 y^2)(x^2+y^2) + \cdots, \tag{36}$$

being

$$\begin{aligned}
\omega =& b_x\sqrt{\frac{b_x^2-1}{b_z}},\\
\alpha_1 =& \pm\frac{b_x^3\sqrt{b_x^2-1}}{2b_z},\\
\alpha_2 =& \frac{b_x^3(b_x^2-1)}{b_z},\\
\beta_1 =& -\frac{b_x^2(b_x^6+4b_z^2+b_x^2(1-9b_z^2)+b_x^4(4b_z^2-2))}{8b_z^3},\\
\beta_2 =& \pm\frac{b_x^2(1-2b_x^2)\sqrt{b_x^2-1}}{b_z},\\
\beta_3 =& -\frac{b_x^2(b_x^6-4b_z^2-2b_x^4(1+6b_z^2)+b_x^2(1+15b_z^5))}{8b_z^3},
\end{aligned} \tag{37}$$

where the plus and minus signs in $\alpha_1$ and $\beta_2$ correspond to $P_5$ and $P_6$ respectively. Note that the presence of different signs in $\alpha_1$ and $\beta_2$ preserves the symmetry of the expansion (36) with respect to the $y$ axis. It can be seen that the linear approximation corresponds to an isotropic harmonic oscillator with frequency $\omega$, which vanishes at $b_x = 1$ and grows monotonically for increasing $b_x$.

Now, we can proceed in the same way as in the previous case, obtaining an averaged Hamiltonian retaining most of the main features of the original system. However, looking at the coefficients in (37), we observe that the smallness of each order in the Taylor series expansion can be altered if $b_x$ is great enough. In this way, the perturbation approach will be only valid in a small neighborhood around the critical points, namely in a ball $B_r$ of radius $r$, centered at $(0,0,0,0) \in \mathbb{R}^4$, with $r$ a function of $b_x$, where it is guaranteed that the terms in the Taylor expansion are properly ordered. With this restriction in mind, the normalization, or averaging process, is accomplished in the same way as previously, up to second order. By doing so, in Lissajous variables, the normalized Hamiltonian is given by:

$$\begin{aligned}
\mathcal{K} = b_z + \omega_o L + \frac{9(\beta_1+\beta_3)\omega_o^2 - 25(\alpha_1^2+\alpha_2^2)}{12\omega_o^4}L^2 + \frac{\alpha_1^2+\alpha_2^2-(\beta_1+\beta_3)\omega_o^2}{4\omega_o^4}G^2 + \\
\frac{20(\alpha_1^2+\alpha_2^2)-9(\beta_1-\beta_3)\omega_o^2}{12\omega_o^4}L^2 e\cos 2g + \frac{40\alpha_1\alpha_2-9\beta_2\omega_o^2}{12\omega_o^4}L^2 e\sin 2g.
\end{aligned} \tag{38}$$

Due to the fact that $g$ is not defined for $|G| = L$, we introduce the Hopf variables (26) and the phase space turns to be a unit radius sphere. In these variables, and after dropping the constant terms, the Hamiltonian becomes

$$\mathcal{K} = a_1\xi_1 + a_2\xi_2 + a_3\xi_3^2,$$

where

$$a_1 = \frac{9 - 2b_x^2 - 2b_x^4}{12(b_x^2 - 1)} L^2, \quad a_2 = \mp \frac{9 + 2b_x^2}{12\sqrt{b_x^2 - 1}} L^2, \quad a_3 = \frac{b_x^2(b_x^2 - 1)}{16 b_z^2} L^2. \tag{39}$$

The upper sign in $a_2$ stands for $P_5$ and the lower one for $P_6$. Taking into account that $a_3 > 0$, if $b_x > 1$, we can divide by this coefficient and consider the biparametric quadratic Hamiltonian

$$\mathcal{K} = \xi_3^2 + c_1 \xi_1 + c_2 \xi_2, \tag{40}$$

being $c_1 = a_1/a_3$ and $c_2 = a_2/a_3$. It is worth noting that an equivalent transformation, a suitable rotation around the $\xi_3$ axis, converts (40) into (27), so we expect a very similar behavior. Indeed, from the equations of the motion arising from Hamiltonian (40) the following equilibria result:

$$\epsilon_1 = \left( \frac{c_1}{\sqrt{c_1^2 + c_2^2}}, \frac{c_2}{\sqrt{c_1^2 + c_2^2}}, 0 \right),$$
$$\epsilon_2 = \left( \frac{-c_1}{\sqrt{c_1^2 + c_2^2}}, \frac{-c_2}{\sqrt{c_1^2 + c_2^2}}, 0 \right),$$
$$\epsilon_{3,4} = \left( \frac{c_2}{2}, \frac{c_1}{2}, \pm \frac{\sqrt{4 - c_1^2 - c_2^2}}{2} \right).$$

While $\epsilon_{1,2}$ always exist, $\epsilon_{3,4}$ exist if the condition

$$\gamma = 4 - c_1^2 - c_2^2 > 0$$

is fulfilled. Therefore, when $\gamma = 0$, equilibria $\epsilon_{3,4}$ and $\epsilon_1$ coincide, and a pitchfork bifurcation is expected, provided that for $\gamma < 0$ only $\epsilon_1$ survives. The equilibria $\epsilon_{1,2}$ correspond to rectilinear orbits which coordinates in the $(g, G/L)$ variables are $\epsilon_1 = (1/2 \arctan(c_2/c_1), 0) \equiv (\pi + 1/2 \arctan(c_2/c_1), 0)$ and $\epsilon_2 = ((\pi + \arctan(c_2/c_1))/2, 0) \equiv ((3\pi + \arctan(c_2/c_1))/2, 0)$. These rectilinear orbits are perpendicular each other. When they exist, the equilibria $\epsilon_{3,4}$ correspond to elliptical orbits with $g = 1/2 \arctan(c_1/c_2) \equiv \pi + 1/2 \arctan(c_1/c_2)$ traveled in direct and retrograde senses, respectively. Finally, it is important noticing that $\epsilon_{1,2,3,4}$ for $c_2 < 0$ and for $c_2 > 0$ (i.e., when they are considered located at the potential well around $P_4$ and at the potential well around $P_5$, respectively) are symmetric with respect to the $y$ axis.

Regarding the linear stability of the equilibrium points, from the characteristic equation

$$\lambda^2 + c_1^2 + c_2^2 + \xi_3^2 - 2c_1\xi_1 - 2c_2\xi_2 = 0,$$

| Point | Eigenvalues | Stability |
|---|---|---|
| $\epsilon_1$ | $\pm\sqrt{2\sqrt{c_1^2+c_2^2}-c_1^2-c_2^2}$ | Stable if $\gamma = 4-c_1^2-c_2^2 < 0$ |
| $\epsilon_2$ | $\pm i\sqrt{2\sqrt{c_1^2+c_2^2}+c_1^2+c_2^2}$ | Always stable |
| $\epsilon_{3,4}$ | $\pm i\sqrt{4-c_1^2-c_2^2}$ | Stable when they exist for $\gamma = 4-c_1^2-c_2^2 > 0$ |

Table III. Linear stability of the equilibrium points for the normalized Hamiltonian $\mathcal{K}$, when $b_x > 1$.

it is straightforward to obtain the eigenvalues associated to each point, which are given in Table III. We can observe that, as we said, there is a pitchfork bifurcation when $\gamma = 0$. In fact, if $\gamma > 0$, the points $\epsilon_{2,3,4}$ are stable while $\epsilon_1$ is a saddle. When $\gamma = 0$, the points $\epsilon_{3,4}$ and $\epsilon_1$ collide and the bifurcation takes place. After that, only $\epsilon_1$ and $\epsilon_2$ exist as stable equilibrium points of center type. Thus, $\gamma = 0$ defines a bifurcation curve in the parameter plane $(b_x, b_z)$, delimiting the regions where two or four equilibrium points exist. These regions are depicted in Fig. 16, being the blue area the region where four equilibrium points exist.

In order to show the evolution of the phase flow, as we did in the case $0 < b_x < 1$, we fix $b_z = 0.1$ and we vary $b_x$. In other words, we follow the black dashed line that appears in Fig.16. Due to the symmetry of the system around the $y$ axis, the phase flow around $P_4$ and around $P_5$ is qualitatively the same and, for simplicity, we reduce to the case around the minimum $P_5$. For $b_z = 0.1$ the pitchfork bifurcation takes place when $\gamma = 0$ at the critical value $b_x \approx 1.0894$. Then, we vary $b_x$ from 1 up to 1.25. In Fig.17 the phase flow evolution of the normalized Hamiltonian $\mathcal{K}$ (40) on the Hopf sphere for $b_x$ =1.05, 1.1 and 1.25 is shown. When $b_x$ is below the critical value $b_x \approx 1.0894$ (see the first row of Fig.17 for $b_x = 1.05$), the phase flow is made of quasiperiodic orbits around the stable equilibria $\epsilon_{1,2}$ that, we remind, they correspond to rectilinear orbits. Furthermore, the nearer an orbit is to $\epsilon_1$ ($\epsilon_2$), the greater its orientation is along $\epsilon_1$ ($\epsilon_2$). At $b_x = 1.1$, the pitchfork bifurcation occurred, so that $\epsilon_1$ becomes unstable, and from it, the stable equilibria $\epsilon_{3,4}$ born (see the second row of Fig.17). The new kind of levels around $\epsilon_{3,4}$ and inside the separatrix passing through $\epsilon_1$ correspond to quasiperiodic orbits with the same symmetry pattern as $\epsilon_{3,4}$, that we remind are elliptical orbits. For increasing values of $b_x$ (see the third row of Fig.17 for

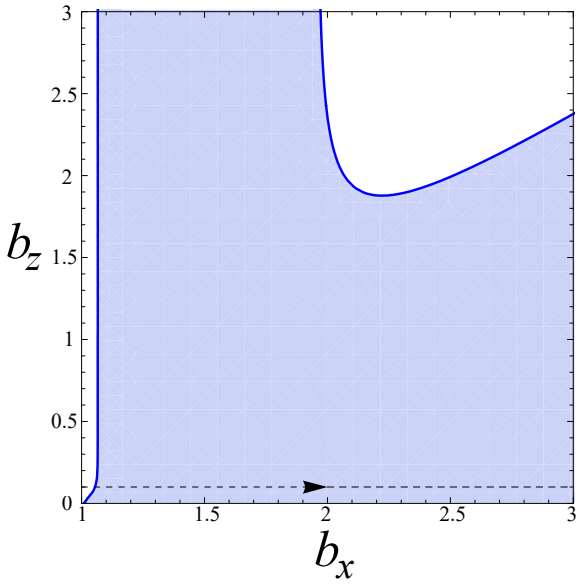


FIG. 16. Bifurcation curve $\gamma = 4 - c_1^2 - c_2^2 = 0$ in the $(b_x, b_z)$ plane. The blue region corresponds to the existence of four equilibrium points. The black dashed line indicates the path used for the numerical investigation of the phase flow structure.

$b_x = 1.25$), equilibria $\epsilon_{3,4}$ move towards the north and the south poles and the phase space around them grows in size.

### B. Phase Flow Structure: $b_x > 1$

In this subsection we focus on the structure and evolution of the phase flow when $b_x > 1$. For this case, the section given by $p_y = 0$ with $\dot{p}_y \geq 0$ is a more convenient Poincaré map because, for $b_x > 1$, trapped motion takes place in the symmetric potential wells around the minima $P_{5,6}$.

We start this study fixing the energy $E = 0.105$ and the value $b_z = 0.1$, while we vary the value of $b_x$. The result of this study is illustrated in Fig.18 for the particular values $b_x = 1.05$, 1.1 and 1.25. Because for these values of $b_x$ the energy $E = 0.105$ is below the energy $E_2 = \sqrt{(1-b_x)^2 + b_z^2} \approx 0.1414$ of the saddle point $P_2$, in all cases the Poincaré section is made of two (symmetric) disjoint regions.

For $b_z = 0.1$ and $b_x = 1.05$, the system is below the critical value $b_x \approx 1.0894$ predicted by the bifurcation curve $\gamma = 0$ shown in Fig.16. The corresponding surface of section (see

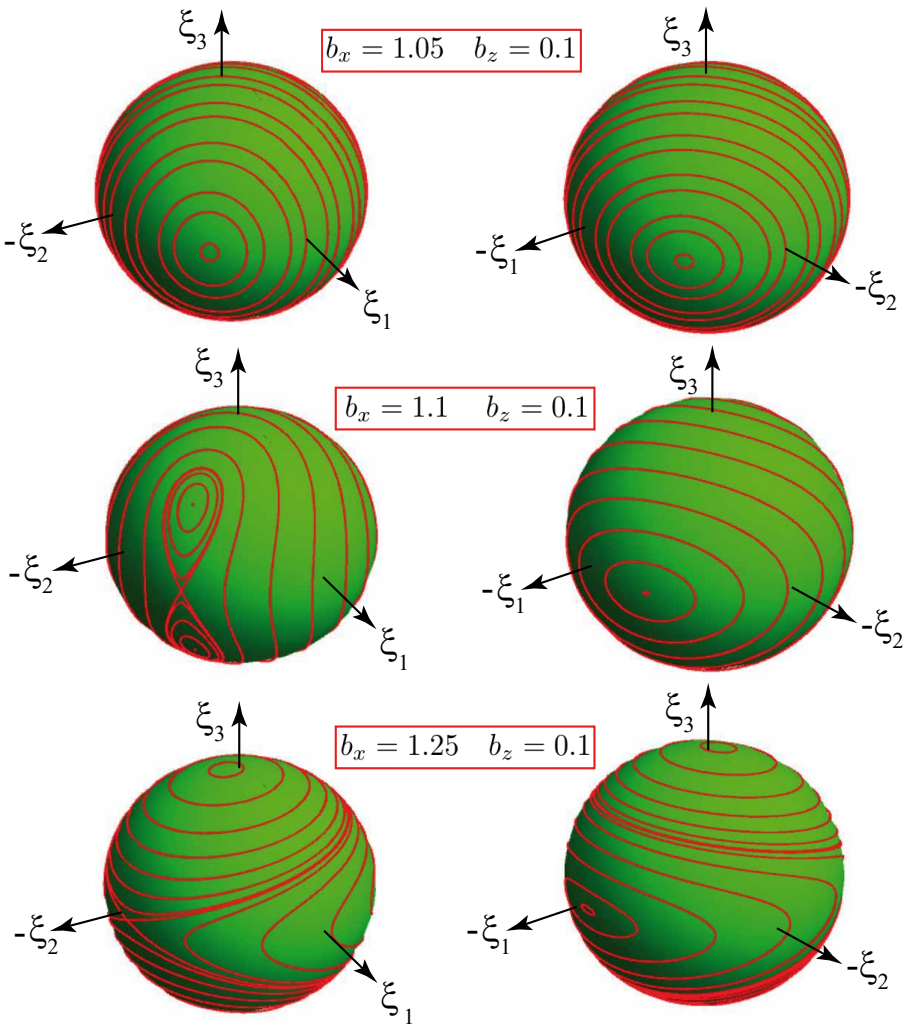


FIG. 17. Phase flow evolution of the of the normalized system corresponding to the dynamics in the symmetric potential wells when $b_x > 1$.

Fig.18(a)) shows that the phase space in each region is ordered around two stable fixed points named as $I_S$ and $I_U$. These fixed points correspond to two linear periodic orbits which are depicted in Fig.19(a)-(b). For $b_x = 1.1$, the system crossed the critical value $b_x \approx 1.0894$, and a pitchfork bifurcation is expected. Indeed, in the second row of Fig.18, we observe that the phase space shows a different structure due to such a bifurcation: From $I_U$, which has become unstable, two stable fixed points, named as $I_C$, born. Periodic orbits $I_C$ are illustrated in Fig.19(c)-(d). For increasing values of $b_x$ (see the Fig.18(c) for $b_x = 1.25$), we observe that, although the phase space structure remains qualitatively the same, there is a significant increase in size of the regions around $I_S$ and $I_C$. Because the energy $E = 0.105$

is close to the energy $E_{5,6} = b_z = 0.1$ of the minima $P_{5,6}$, we remark the perfect matching between the number and stability of the (non-degenerate) equilibria in the averaged system (see Fig.17) and the number and stability of the periodic orbits in the original one.

Now, we study the impact of the energy in the phase flow. In this way, using the Poincaré map $p_y = 0$ with $\dot{p}_y \geq 0$, we fix the values $b_x = 1.25$ and $b_z = 0.1$ while we increase the energy. For $E = 0.2$ the system is below the energy $E_2 = \sqrt{(1-b_x)^2 + b_z^2} \approx 0.2693$ of the saddle $P_2$, and the corresponding Poincaré section shown in Fig.20(a) is made of two disjoint regions with the same structure as we found in Fig.18(b)-(c),with all the orbits ordered around the fixed points $I_{C,S,U}$.

When the energy approaches the saddle point energy $E_2 \approx 0.2693$ (see Fig.20(b)-(c) for $E = 0.25$ and for $E = 0.265$), the system begins to lose its regular behavior, so that there appear large regions of chaotic motion that embed number chains of island of regular motion. When the energy is above $E_2 = \sqrt{(1-b_x)^2 + b_z^2} \approx 0.2693$, the surface of section is made of only one region (see Fig.20(d) for $E = 0.28$) and a significant region of phase space is dominated by chaotic motion. It is worth noticing that the orbits in the phase space regions around the periodic orbits $I_C$ show a very robust regular motion.

## VI. CONCLUSIONS

We have analyzed the behavior of a neutral atom in a trap induced by a two-wire waveguide in the presence of two bias magnetic fields, $b_x$ and $b_z$. Assuming that the wires and the external fields are located according to Fig.1, the trapping region appears in the $x$-$y$ plane.

Because most of the atom trapping features are determined by the landscape of the potential energy surface, we start our study by analyzing its critical points. When the two bias fields are zero, there is only one trapping region around the origin (see Fig. 2). When the bias fields are non-zero, the number of critical points increases and so do the trapping regions.

When $b_z > 0$ and $0 < b_x < 1$, two trapping regions (potential wells) appear on the $y$ axis (see Fig. 3). Because the outer potential well (around the minimum $P_4$) is much wider than the inner one (around the minimum $P_1$), a tighter binding is associated to the latter. We have used perturbation theory to describe the dynamics when the atom is trapped in these potential wells. More precisely, the Taylor expansion of the potential

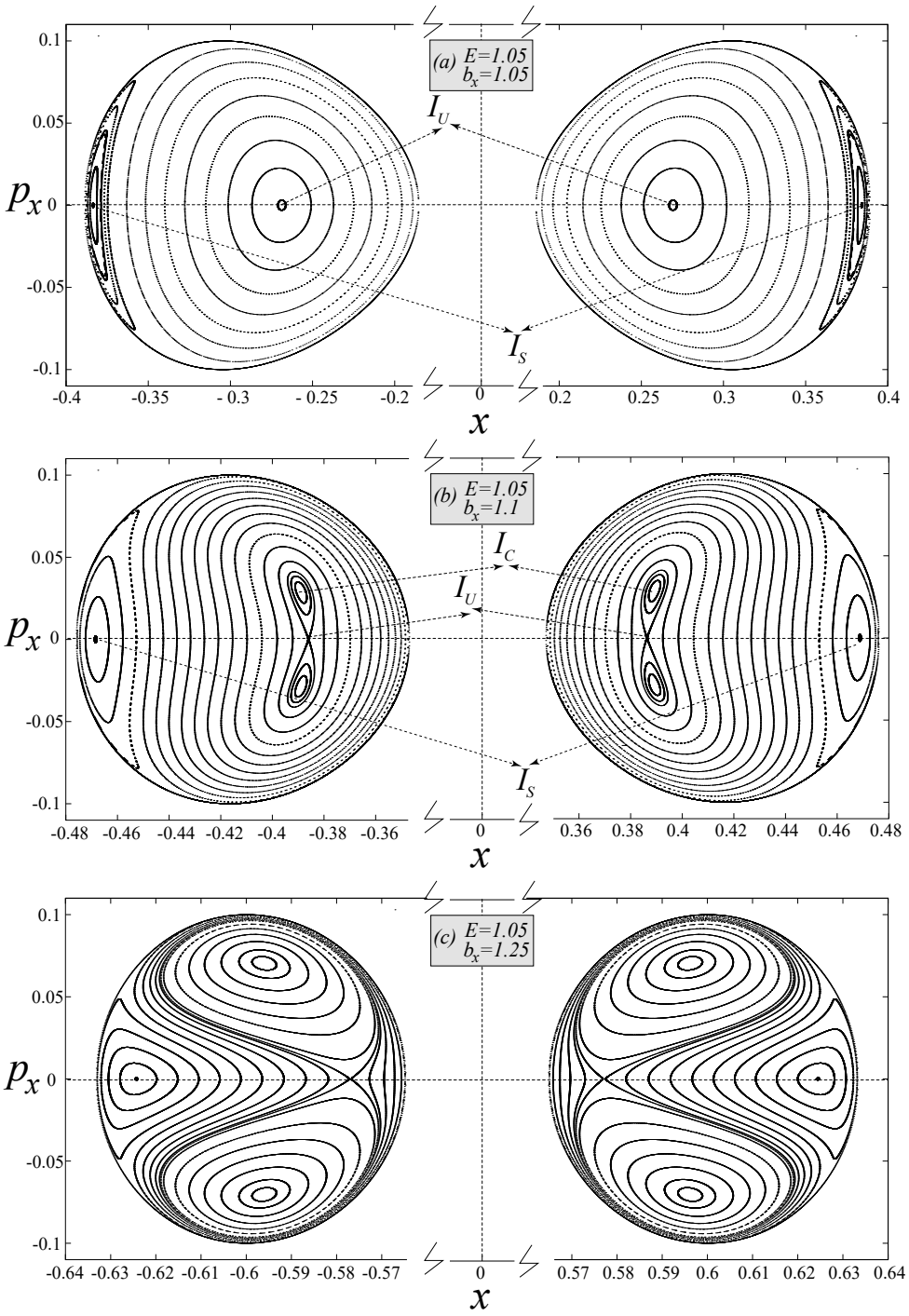


FIG. 18. Poincaré section $p_y = 0$ with $\dot{p}_y \geq 0$ for $b_x = 1.05$, $b_x = 1.1$ and $b_x = 1.25$, and for the energy $E = 1.05$ and $b_z = 0.1$. Because the energy $E = 1.05$ is below the energy $E_2 \approx 0.1414$ of saddle point $P_2$, the Poincaré section is made of two (symmetric) disjoint regions.

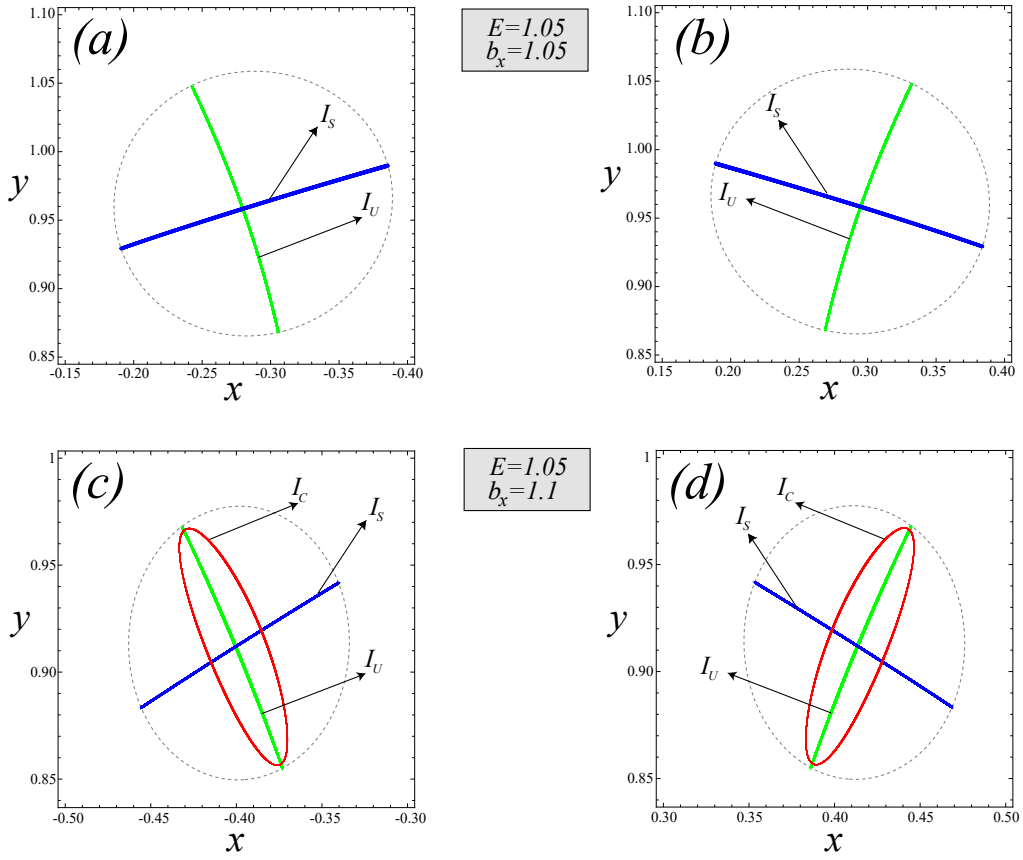


FIG. 19. Periodic orbits $I_S$, $I_U$ and $I_C$. All orbits for $b_z = 0.1$ and for the energy $E = 0.105$. The black dotted lines are the corresponding equipotential curves $E = V(x, y) = 0.105$.

around the $P_{1,4}$ shows that the system behaves as a perturbed two-dimensional isotropic oscillator. The linear approximation confirms that the dynamics is, in general, much faster in the inner potential well (i.e., around $P_1$) than in the outer one (i.e., around $P_4$), see Fig. 5. For the perturbation process, we use the Lissajous transformation which provides us an integrable (normalized) Hamiltonian truncated at order 2. Expressed in Hopf variables, the phase space consists of a unit radius sphere, and the normalized Hamiltonian appears as a quadratic polynomial depending on two parameters, $a_1$ and $a_2$, which are functions of $b_x$, $b_z$. We find that the critical value $|a_1| = (2a_2)$, see Fig. 7, determines the dynamics because it defines a bifurcation curve that divides the parameter plane $(b_x, b_z)$ into different regions where the number of equilibrium points (and their stability character) changes from two to four. Although the bifurcation curve $|a_1| = (2a_2)$ is different for the inner well than for the outer one, bifurcations are always of pitchfork-type, see Fig. 7 and Fig. 8. The evolution of the phase flow on the Hopf spheres perfectly agrees with the Poincaré surfaces of section

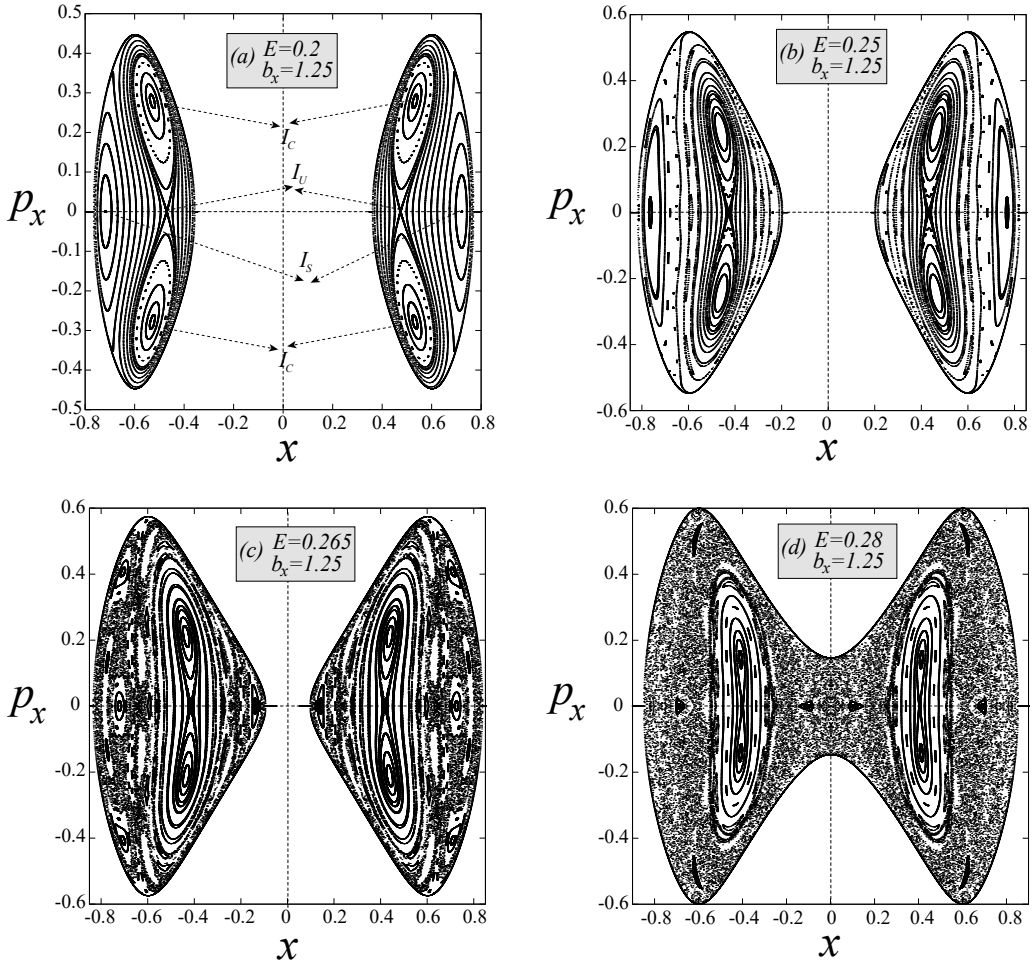


FIG. 20. Poincaré section $p_y = 0$ with $\dot{p}_y \geq 0$ for $b_x = 1.25$, $b_z = 0.1$ and for energy values $E = 0.2$, $E = 0.25$, $E = 0.265$ and $E = 0.28$. When the energy $E$ of the system is above the energy $E_2 \approx 0.2693$ of the saddle point $P_2$, the Poincaré section is made of only one region (see panel (d)).

accounting for the evolution of the original system (see Fig. 8, Fig. 10 and Fig. 11).

When $b_x = 1$ the equilibria $P_1$, $P_2$ and $P_4$ collide, there is a bifurcation and for $b_x > 1$ two symmetric trapping regions appear on the unit circle, see Fig. 4. They are associated to the new-born equilibria $P_5$ and $P_6$. The dynamics around these (symmetric and equivalent) equilibria is studied following the same scheme as for $0 < b_x < 1$. Because, the linear approximation corresponds to an isotropic oscillator, we follow the same perturbation procedure as for $b_x < 1$. Indeed, we obtain again that the averaged Hamiltonian expressed in Hopf variables is a quadratic polynomial depending on two parameters, $c_1$ and $c_2$, that are functions of $b_x$, $b_z$. The bifurcation curve $4 - c_1^2 - c_2^2 = 0$ divides the parameter plane $(b_x, b_z)$ into

different regions where the number of equilibrium points changes from two to four through bifurcations of pitchfork-type, see Fig. 16. We find a perfect agreement between the evolution of the phase flow on the Hopf spheres and the Poincaré surfaces of section accounting for the evolution of the original system (see Fig. 17 and Fig. 18). As expected, when the energy of the system increases and gets closer to the one of the saddle points that determine the potential wells, the Poincaré sections show that chaos appears and begins to dominate.

Although it is beyond the scope of this paper, the results of our study can be a guideline to carry out investigations concerning the frontier between classical and quantum dynamics in a realistic system. For example, the low dimensionality of Hamiltonian (9) makes our model very suitable for studying dynamical tunneling effects [49]. We also note that the normalized Hamiltonians (25) and (38) obtained after the Lissajous transformation are amenable to semiclassical quantization (see e.g. [47, 48]) using the well-known Einstein–Brillouin–Keller quantization conditions. Finally, due to our system shows a transition from regular to chaotic behavior, the fundamental question of the quantum signatures of classical chaos can be investigated using this model. Work along these lines is now in progress.

## ACKNOWLEDGEMENTS

This work has been partly supported from the Spanish Ministry of Science and Innovation through the Project MTM2017-88137-CO (Subprojects MTM2017-88137-C2-1-P and MTM2017-88137-C2-2-P), and by University of La Rioja through Projects REGI 2018751 and REGI 2020/15.

[1] A. L. Migdall, J. V. Prodan, W. D. Phillips, T. H. Bergeman, and H. J. Metcalf, Phys. Rev. Lett. **54** 2596 (1985). First Observation of Magnetically Trapped Neutral Atoms.

[2] M. H. Anderson, J. R. Ensher, M. R. Matthews, C. E. Wieman, E. A. Cornell, Science **269**, 198 (1995). Observation of Bose-Einstein condensation in a dilute atomic vapor.

[3] K. B. Davis, M.-O. Mewes, M. R. Andrews, N. J. van Druten, D. S. Durfee, D. M. Kurn, W. Ketterle, Phys. Rev. Lett. **75**, 3969 (1995). Bose-Einstein Condensation in a Gas of Sodium Atoms.

[4] C. C. Bradley, C. A. Sackett, R. G. Hulet, Phys. Rev. Lett. **78**, 985 (1997). Bose-Einstein Condensation of Lithium: Observation of Limited Condensate Number.

[5] W. Ketterle, D. S. Durfee, and D. M. Stamper-Kurn, *Bose-Einstein Condensation in Atomic Gases (Proceedings of the International School of Physics)*, eds. M. Inguscio, S. Stringari and C. E. Wieman ( Societa Italiana Di Fisica, 1999).

[6] H. J. Metcalf, P. van der Straten, *Laser Cooling and Trapping* (Springer-Verlag, New York, 1999).

[7] C. Monroe, E. Cornell, C. Wieman, in Proceedings of the International School of Physics, edited by E. Arimondo, W. D. Phillips, F. Strumia (North-Holland, Amsterdam, 1993), pp. 361–378

[8] T. Bergeman, G. Erez and H. J. Metcalf, Phys. Rev. A, **35**, 4, 1535 (1987). Magnetostatic trapping fields for neutral atoms.

[9] W. Paul, Rev. Mod. Phys. **62**, 531 (1990). Electromagnetic traps for charged and neutral particles.

[10] D. E. Pritchard, Phys. Rev. Lett. **51**, 1336 (1983). Cooling Neutral Atoms in a Magnetic Trap for Precision Spectroscopy.

[11] Eur. Phys. J. D **35** (2005). Special Issue: Atom chips: manipulating atoms and molecules with microfabricated structures.

[12] J. Fortágh and C. Zimmermann, Rev. Mod. Phys. **79**, 235 (2007). Magnetic microtraps for ultracold atoms.

[13] J. Schmiedmayer, Phys. Rev. A **52**, R13-R16 (1995). Guiding and trapping a neutral atom on a wire.

[14] J. Schmiedmayer, Appl. Phys. B **60**, 169 (1995). A wire trap for neutral atoms.

[15] J. Fortagh, A. Grossmann, and C. Zimmermann and T. W. Hänsch, Phys. Rev. Lett. **81**, 5310 (1998). Miniaturized Wire Trap for Neutral Atoms.

[16] J. Denschlag, D. Cassettari and J. Schmiedmayer, Phys. Rev. Lett. **82**, 2014 (1999). Guiding Neutral Atoms with a Wire.

[17] R. Folman, P. Krüger, J. Schmiedmayer, J. Denschlag, and C. Henkel, Advances in Atomic, Molecular, and Optical Physics **48**, 263 (2002). Microscopic atom optics: from wires to an atom chip.

[18] A. E. Leanhardt, A. P. Chikkatur, D. Kielpinski, Y. Shin, T. L. Gustavson, W. Ketterle, and D. E. Pritchard, Phys. Rev. Lett. **89**, 040401 (2002). Propagation of Bose-Einstein Condensates in a Magnetic Waveguide.

[19] H. Ott, J. Fortagh, S. Kraft, A. Günther, D. Komma, and C. Zimmermann, Phys. Rev. Lett. **91**, 040402 (2003). Nonlinear Dynamics of a Bose-Einstein Condensate in a MagneticWaveguide.

[20] D.-W. Wang, M. D. Lukin, and E. Demler, Phys. Rev. Lett. **92**, 076802 (2004). Disordered Bose-Einstein Condensates in Quasi-One-Dimensional Magnetic Microtraps.

[21] S. Aubin, S. Myrskog, M. H. T. Extavour, L. J. LeBlanc, D. McKay, A. Stummer, and J. H. Thywissen, Nat. Phys. **2**, 384 (2006). Rapid sympathetic cooling to Fermi degeneracy on a chip.

[22] M. Singh, M. Volk, A. Akulshin, A. Sidorov, R. McLean and P. Hannaford, J. Phys. B: At. Mol. Opt. Phys. **41**, 065301 (2008). One dimensional lattice of permanent magnetic microtraps for ultracold atoms on an atom chip.

[23] I. Herrera, Y. Wang, P. Michaux, D. Nissen, P. Surendran, S. Juodkazis, S. Whitlock, R. J. McLean, A. Sidorov, M. Albrecht, P. Hannaford, J. Phys. D: Appl. Phys. **48**, 115002 (2015). Sub-micron period lattice structures of magnetic microtraps for ultracold atoms on an atom chip.

[24] T. Bergeman. Personal communication.

[25] V. Gomer, O. Harms, D. Haubrich, H. Schadwinkel, F. Strauch, B. Ueberholz, S. aus der Wiesche, D. Meschede, Hyperfine Interact. **109**, 281 (1997). Magnetostatic traps for charged and neutral particles.

[26] J. P. Salas and M. Iñarrea, Eur. Phys. J. D **67**, 248 (2013). Regular and chaotic dynamics of a neutral atom in a magnetic trap.

[27] E. L. Surkov, J. T. M. Walraven, G. V. Shlyapnikov, Phys. Rev. A **49**, 4778 (1994). Collisionless motion of neutral particles in magnetostatic traps

[28] M. Lenz, S. Wüster, C. J. Vale, N. R. Heckenberg, H. Rubinsztein-Dunlop, C. A. Holmes, G. J. Milburn, and M. J. Davis, Phys. Rev. A **88**, 013635 (2013). Dynamical tunneling with ultracold atoms in magnetic microtraps.

[29] C. L. Garrido Alzar, Phys. Rev. A **97**, 033405 (2018). Stability analysis of a magnetic waveguide with self-generated offset field. Dynamical tunneling with ultracold atoms in magnetic

microtraps.

[30] E. A. Hinds, C. J. Vale, and M. G. Boshier, Phys. Rev. Lett. **86**, 1462 (2001). Two-wire waveguide and interferometer for cold atoms.

[31] E. Majorana, Nuovo Cimento **9**, 43 (1932). Atomi orientati in campo magnetico variabile.

[32] D. M. Brink and C. V. Sukumar, Phys. Rev. A **74**, 035401 (2006). Majorana spin-flip transitions in a magnetic trap.

[33] R. Abraham, J. E. Marsden, Foundations of Mechanics (Benjamin/Cummings, Reading MA, 1980).

[34] B. R. Miller, Celestial Mech. Dyn. Astr. **51**, 251 (1991). The Lissajous transformation. III Parametric bifurcations.

[35] A. Deprit and A. Elipe, Celestial Mech. Dyn. Astr. **51**, 227 (1991). The Lissajous transformation. II Normalization.

[36] A. Elipe, B. Miller and M. Vallejo, 1995, Astron. Astrophys. **300**, 722-725 (1995). Bifurcation in a non-symmetric cubic potential.

[37] A. Deprit, Celest. Mech. Dyn. Astr. **51**, 201 (1991). The Lissajous transformation. I Basics.

[38] A. Deprit, Celest. Mech. **1**, 12 (1969). Canonical Transformations Depending on a Small Parameter.

[39] A. Deprit, S. Ferrer, Rev. Acad. Ciencias Zaragoza **45**, 111 (1990). On the Polar Orbits of the Zeeman Effect in a Moderately Strong Magnetic Field.

[40] A. Elipe and V. Lanchares, Mech. Res. Comm. **21**, 209, 1994. Biparametric quadratic Hamiltonians on the unit sphere: Complete classification.

[41] V. Lanchares and A. Elipe, Chaos **5**, 367, 1995. Bifurcations in biparametric quadratic potentials.

[42] V. Lanchares and A. Elipe, Chaos, **5**, 531, 1995. Bifurcations in biparametric quadratic potentials. II.

[43] J. E. Howard, R. S. Mackay, Phys. Lett. A **122**, 331 (1987). Calculation of linear stability boundaries for equilibria of Hamiltonian systems.

[44] J. E. Marsden, T. S. Ratiu, *Introduction to Mechanics and Symmetry*, Text in Applied Mathematics 17 (Springer, New York, 1994)

[45] E. A. Coddington, N. Levinson, *Theory of Ordinary Differential Equations* (McGraw Hill, New York, 1995).

[46] G. Reeb, Acad. Roy. Belgique. Cl. Sci. Mém. Coll. in 8°. 27 article 9 (1952). Sur certaines propriétés topologiques des trajectoires des systémes dynamiques.

[47] M. Iñarrea and J. P. Salas, Eur. Phys. J. D **27**, 3 (2003). Rydberg hydrogen atom in the presence of uniform magnetic and quadrupolar electric fields. A quantum mechanical, classical and semiclassical approach.

[48] C. Jaffé, J. Palacián, P. Yanguas and T. Uzer, Theor. Chem. Acc. **134**, 1592 (2015). Semiclassical quantization of atomic systems through their normal form: the hydrogen atom.

[49] M. J. Davis and E. J. Heller, J. Chem. Phys. **75**, 246 (1981). Quantum dynamical tunneling in bound states .